

# **Fabrication of Clean Iron Nanostructures on Silicon Oxide via Focused Electron Beam Induced Processing in UHV**

**Untersuchungen zur Herstellung von sauberen Eisen-  
Nanostrukturen auf Siliziumoxid mittels Fokussierter  
Elektronenstrahl-induzierter Prozessierung im UHV**

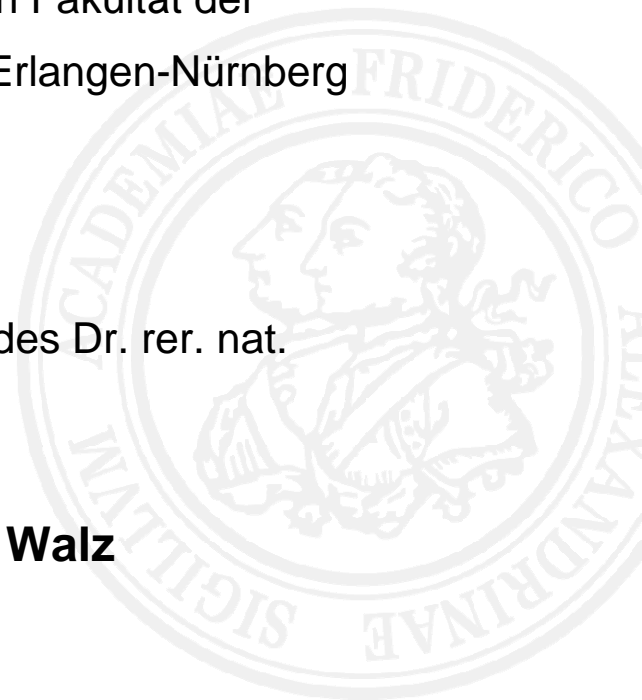
Der Naturwissenschaftlichen Fakultät der  
Friedrich-Alexander-Universität Erlangen-Nürnberg

zur Erlangung des Doktorgrades Dr. rer. nat.

vorgelegt von

**Marie-Madeleine Walz**

aus Erlangen



Als Dissertation genehmigt  
durch die Naturwissenschaftliche Fakultät  
der Friedrich-Alexander-Universität Erlangen-Nürnberg

Tag der mündlichen Prüfung: 24.04.2012

Vorsitzende/r der Promotionskommission: Prof. Dr. Rainer Fink  
Erstberichterstatter/in: Prof. Dr. Hans-Peter Steinrück  
Zweitberichterstatter/in: Priv. Doz. Dr. Norbert Jux

## Abstract

Going from the macroscopic to the nanometer scale, materials exhibit new and promising properties, which are not observed on larger length scales. Therefore, the fabrication of nanoscaled structures on surfaces, with precise location and controlled chemical composition, is of high interest e.g. for the semiconductor industry. This issue is addressed by the focused electron beam induced processing (FEBIP) techniques.

This thesis aimed at the fabrication of clean iron nanostructures from the precursor iron pentacarbonyl,  $\text{Fe}(\text{CO})_5$ , on insulating silicon oxide substrates via FEBIP techniques with successive autocatalytic growth at room temperature in ultra-high vacuum (UHV). The nanostructures were characterized by scanning electron microscopy and local Auger electron spectroscopy.

Starting from electron beam induced deposition (EBID) followed by autocatalytic growth on thermal 300 nm  $\text{SiO}_x$  on Si(001), a novel lithographic technique was developed: electron beam induced surface activation (EBISA). This novel FEBIP technique relies on the local dissociation of  $\text{Fe}(\text{CO})_5$  at electron pre-irradiated regions. The mechanistic understanding of this process was furthered on *in situ* prepared thermal ultra-thin  $\text{SiO}_x$  (0.5 nm) on Si(001). It was proven that understoichiometric silica is the active site for  $\text{Fe}(\text{CO})_5$  dissociation.

The concept of EBISA was also transferred to native silicon oxide on silicon and on silicon nitride. Comparing the latter bulk substrates to silicon nitride membranes, proximity effects were studied for EBISA and EBID. Contrary to the expectation, it was demonstrated that proximity effects can be more pronounced on silicon nitride membranes than on the respective bulk substrates, which was explained by a positive charging effect and thereby induced oxygen desorption beyond the backscattered electron exit area. In addition, it was shown for the silicon nitride membrane that a positive charging of the formed EBI deposit leads to an enhanced deposition rate, exceeding the ones observed on the respective bulk substrates.

In the framework of two cooperations the physical and chemical properties of the generated iron structures were investigated. Electrical- and magnetotransport measurements showed that the iron deposits exhibit metallic conductivity and ferromagnetic magnetization properties as expected from clean iron thin films. In these studies, the phenomenon of the inhibition of autocatalytic growth by chromium oxide was observed, which is another “tool in the box” to tune the morphology of nanostructures. Finally, it is reported that EBISA Fe nanostructures can be utilized as a catalyst for the local growth of silicon nanowires via high temperature chemical vapor deposition.

---

---

## Contents

1.	Introduction .....	1
2.	Fundamentals & techniques.....	5
2.1.	Scanning electron microscopy (SEM).....	5
2.2.	Auger electron spectroscopy (AES).....	7
2.3.	Quadrupole mass spectrometry (QMS) .....	9
2.4.	Low energy electron diffraction (LEED) .....	10
2.5.	Electron beam induced lithographic techniques .....	11
2.5.1.	Electron beam induced deposition (EBID) .....	11
2.5.2.	Electron beam induced surface activation (EBISA) .....	14
2.5.3.	Autocatalytic growth .....	16
2.5.4.	Lithographic control.....	18
2.6.	Investigated surfaces & precursor molecule .....	19
2.6.1.	Silicon oxide on silicon and silicon nitride .....	19
2.6.2.	Iron pentacarbonyl (Fe(CO) <sub>5</sub> ).....	20
2.7.	UHV instrument.....	20
3.	Results .....	23
3.1.	Local pre-activation with electrons.....	23
3.2.	On the nature of the activated sites .....	29
3.3.	Investigation of proximity effects for EBISA and EBID.....	33
3.4.	Fabrication of Fe deposits for electrical- & magnetotransport measurements...41	
3.5.	Fe nanostructures as catalyst for Si nanowire growth .....	47
4.	Summary .....	51
5.	Outlook.....	55
6.	Zusammenfassung .....	57
7.	Literature .....	61
8.	Abbreviations .....	67
9.	Acknowledgment .....	69
10.	Curriculum Vitae .....	71
11.	Peer-reviewed publications .....	73
12.	Appendix.....	75

---

## 1. Introduction

Nanostructures are already part of our daily life. Silver nanoparticles, applied as an antibacterial agent, titanium oxide nanoparticles, used in transparent sunscreens, or carbon nanotubes, employed for stain-resistant textiles, are of widespread use. Besides these large scale commercial applications, the precise fabrication of nanostructures on surfaces with well-defined chemical composition is still one of the major challenges in semiconductor industry and nanotechnology.

The term nanotechnology is used in general for the fabrication and characterization of structures, materials or devices of a size between 1 to 100 nm, in at least one dimension. On this length scale, the surface-to-volume ratio increases drastically, i.e. the surface properties are more prevailing than the bulk properties of the respective material, and progressively quantum mechanical effects become important, both leading to new and promising properties of nanostructures. The two main strategies for the fabrication of nanostructures are the so-called top-down and bottom-up approaches. While the top-down approach employs larger means (like e.g. an electron beam set-up) to manipulate on a smaller scale, the bottom-up approach uses smaller entities (like e.g. atoms or molecules) to form larger assemblies. [1] The latter approach often relies on self-assembled growth.

A key role in the development of nanotechnology certainly played the construction of novel high resolution microscopes, surpassing the hitherto existing resolution limitations of optical microscopes. Among these high resolution microscopes, electron microscopes were developed in the early thirties of the 20<sup>th</sup> century. [2] Ernst Ruska, one of the inventors, was awarded with the Nobel Prize in Physics in 1986 for his fundamental work in this field and for the construction of the first electron microscope. [3]

Considering the fact that the probe always influences the object of observation, it is clear that it did not take long to actually manipulate matter on the very small scale with the corresponding microscopes. For example, a focused electron beam (from a scanning or a transmission electron microscope, with typical energy values ranging from 10 to 100 keV) is well suited to trigger local chemistry, i.e. to modify physical and / or chemical properties on the nanometer scale; with this approach, focused electron beam induced processing (FEBIP) techniques were developed. Nowadays, scanning electron microscopes (SEMs) are widely available; they are well suited for the field of nanolithography, due to the inherent ability of exact beam positioning and the routinely achievable beam diameters in the nanometer regime. Therefore, very small features can be generated with FEBIP.

## 1. Introduction

---

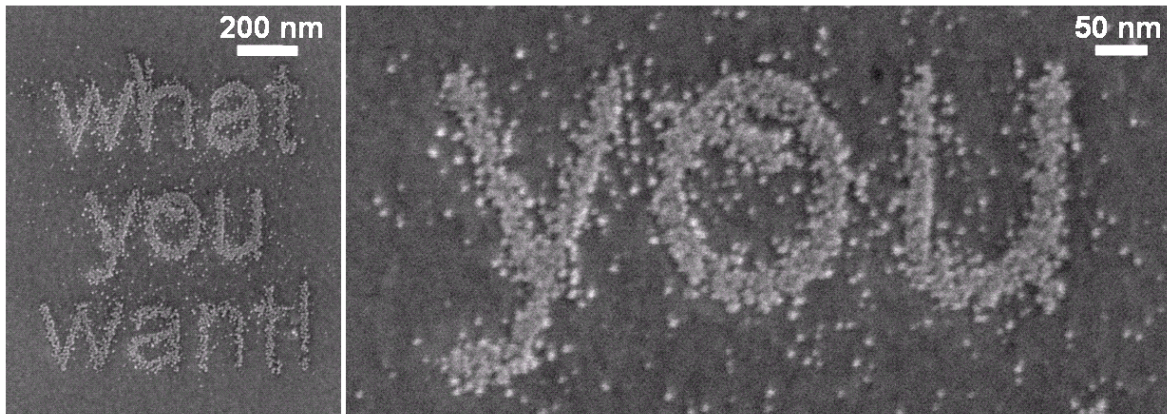


*Figure 1.1 SEM images of Fe nanoclusters (“what you want” logo) deposited via EBID and autocatalytic growth on a SiN-bulk substrate ( $1.7 \mu\text{C}/\text{cm}$ , AGDT = 29 min,  $p(\text{Fe}(\text{CO})_5) = 3.0 \times 10^{-7}$  mbar).*

One method which belongs to this category is the electron beam induced deposition (EBID). Based on EBID, a new FEBIP technique was introduced in the framework of this thesis, named “electron beam induced surface activation” (EBISA), which can also be used for the fabrication of nanostructures on surfaces.

Both methods rely on the focused electron beam in combination with precursor molecules, which allows for the local deposition of arbitrarily shaped nanostructures on surfaces (cf. *Figure 1.1*). In EBID, the deposit is fabricated by direct decomposition of precursor molecules by a focused electron beam. For this technique, the electron beam might be seen as “pen”, and the precursor molecules as “ink”. In addition to the direct deposition of material by the electron beam in EBID, also autocatalytic growth properties of the applied precursor molecule can be employed. For the amount deposited via the autocatalytic growth, the additional gas dosage time (AGDT) is decisive. In EBISA, the surface is locally activated, i.e. chemically modified, by the electron beam such that in a successive step, deposition from the precursor gas occurs at the activated, i.e. catalytically active, sites. This process might be understood as writing with the electron beam as “invisible ink”, which is “developed” by the precursor gas at a later time. Again autocatalytic growth can be employed.

In general, lithographic methods as EBID and EBISA are classified as top-down approaches, as a larger means is utilized to manipulate on a smaller scale. EBISA however, where the initial formation of nuclei is triggered by the catalytic decomposition of the precursor on a surface which was locally activated by an electron beam (top-down) with successive autocatalytic growth (bottom-up), might be considered as a bridging technique between these two approaches.

In contrast to EBISA, which has been up to now solely studied by our research group, EBID is subject to numerous scientific investigations. The smallest EBID structures, fabricated on a membrane, were in the sub-nm-regime. [4] Despite its potentially high resolution, the comparably low speed of fabrication is challenging. This issue is already addressed in the upcoming multiple beam systems. [5] For EBID, a wide variety of chemical compositions of the deposit is accessible, i.e. from insulating to metallic, by choosing the appropriate precursor molecules. However, the purity of these deposits is still one of the major challenges. Often, the co-deposition of carbonaceous residual gases (from e.g. a high vacuum environment) contaminates the deposits. [6-8] To overcome this limitation, a “surface science” approach, i.e. working under ultra-high vacuum (UHV, in the very low  $10^{-10}$  mbar regime) conditions, was applied in this thesis. Thereby, typical contaminants, such as carbon and oxygen, can be drastically reduced. Furthermore, UHV allows for the preparation and the maintenance of clean surfaces, i.e. to work under well defined conditions, which is mandatory at least for EBISA, since this technique relies on the catalytic decomposition at activated sites, which might be deactivated e.g. by carbon contaminations. This underlines that the surface of a substrate is of high importance in FEBIP: besides the impact on adsorption, desorption and diffusion behavior of the precursor, the surface can act as active part in the deposition process itself, as observed e.g. for EBISA.

Another challenge in FEBIP techniques are so-called proximity effects. In the context of EBID and EBISA, these are unintended deposits in close vicinity to the impact point of the focused electron beam due to scattered electrons and thereby induced secondary electrons. EBISA is a method which is perfectly suited to visualize the BSE proximity effect without a superimposed FSE proximity effect; these two proximity effects cannot be separated in EBID.

In this thesis, iron (Fe) nanostructures have been fabricated on various silicon oxide and silicon nitride substrates. The silicon based specimens are of high importance, being the most widespread material in semiconductor industry; well-defined Fe nanostructures are of particular interest due to their potential application in magnetic sensing, data storage and catalysis. They catalyze e.g. the formation of carbon-carbon bonds [9] in the Fischer – Tropsch process [10] or the growth of carbon nanotubes [11, 12]; the latter was also shown by our research group [13].

For the fabrication of Fe nanostructures, the precursor iron pentacarbonyl,  $\text{Fe}(\text{CO})_5$ , was utilized for all experiments presented in the thesis at hand. The autocatalytic growth behavior from this precursor was studied on thermal 300 nm  $\text{SiO}_x$  on Si(001) at room temperature (RT). In the course of these investigations, the new lithographic technique

## 1. Introduction

---

EBISA was established (cf. *Chapter 3.1*). To explore the influence of the thickness of the silicon oxide layer on both lithographic processes, but in particular on EBISA, ultra-thin (~ 0.5 nm) silicon oxide layers were fabricated on Si(001) *in situ*. One goal of these experiments was to elucidate the role of charging and to study the nature of the activated sites in EBISA in more detail (cf. *Chapter 3.2*). Moreover, proximity effects were investigated for EBID and EBISA in dependence of the substrate thickness: silicon nitride (SiN) membranes were studied in comparison to the respective bulk substrates (cf. *Chapter 3.3*). Another aim of these experiments was to expand the EBISA concept to native silicon oxide surfaces. To study the electrical and magnetic properties, Fe microwires were fabricated on 300 nm SiO<sub>x</sub> on Si(001) samples equipped with Au contacts. The corresponding measurements were performed by a cooperation partner from the Goethe University Frankfurt (Prof. Dr. Michael Huth). In the framework of these investigations an interesting phenomenon regarding the inhibition of autocatalytic growth was observed (cf. *Chapter 3.4*). In addition to the physical properties, also the chemical nature of the deposits was explored. By a cooperation partner from the Technical University Vienna (Prof. Dr. Alois Lugstein) it was tested, whether the Fe nanostructures can be employed for the local growth of Si nanowires via high temperature chemical vapor deposition (cf. *Chapter 3.5*). In the *Appendix*, the publications, which contribute to this cumulative PhD thesis, are presented.

## 2. Fundamentals & techniques

### 2.1. Scanning electron microscopy (SEM)

In scanning electron microscopy (SEM) a highly focused electron beam (primary electrons, PEs) is used for the investigation of surfaces and nanostructures by scanning the specimen. The PEs have a certain kinetic energy which is determined by the acceleration voltage ( $E_{PE} = eU$ ). The interaction of the PEs with the sample leads to the emission of electrons and electromagnetic radiation, which can be detected for image acquisition. These micrographs have a high depth of field explaining their typical three-dimensional appearance. A maximum theoretical resolution of 1 – 5 nm can be obtained [14]. One of the basic requirements to perform SEM is that the sample is conductive, i.e. the sample should be metallic or semiconducting. Insulating samples can be investigated via SEM if a coating (e.g. gold) and / or a high background pressure in the SEM chamber (up to the mbar regime) is applied to avoid charging. Still, some non-conducting materials (up to a certain thickness) supported by a conducting or semiconducting substrate, like e.g. 300 nm silicon oxide on Si, can be investigated in standard SEM without interfering charging effects, even though the exact mechanism is not yet fully understood.

Signals which can be acquired for image formation are secondary electrons (SEs), backscattered electrons (BSEs), Auger electrons (AEs) and X-rays, all being emitted from the so-called interaction volume. The two latter signals also bear chemical information; therefore, they can be used for chemical analysis of the sample. While the SEs and the AEs are surface-sensitive, i.e. they are emitted from the top-most surface layers (up to 10 nm [15]), the BSEs and X-rays are more bulk-sensitive, i.e. they are emitted also from below the surface (in the  $\mu\text{m}$  regime). This is due to the different typical kinetic energies of these probes and their inelastic mean free paths. The energies of SEs are defined to be below 50 eV, those of AEs have energies between 50 and 2000 eV and those of BSEs range from 50 eV up to  $E_{PE}$ . The lower energies of the SEs and AEs result in shorter inelastic mean free paths compared to those of the higher energy BSEs or the X-rays.

The broad energy distribution of the BSEs is caused by multiple inelastic scattering of the PEs, which causes multiple energy losses. SEs are generated by inelastic collisions of PEs and BSEs with sample atoms, being emitted either as so-called  $\text{SE}_I$  or as  $\text{SE}_{II}$ , respectively. Based on the rather local emission of  $\text{SE}_I$ s (in the range of the diameter of the impinging PE beam) in comparison to  $\text{SE}_{II}$ s, which are emitted from the whole BSE

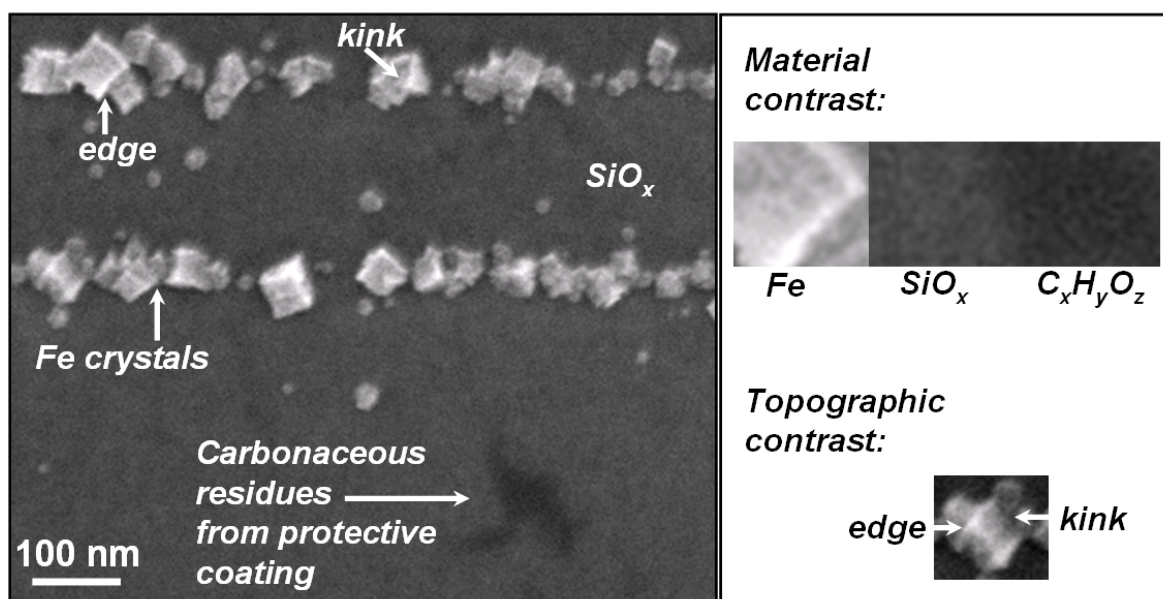


Figure 2.1 SEM image of EBISA Fe nanocrystals lines on 300 nm  $\text{SiO}_x$  on  $\text{Si}(001)$  ( $\sim 0.9 \mu\text{C}/\text{cm}$ ,  $\text{AGDT} = 251 \text{ min}$ ,  $p(\text{Fe}(\text{CO})_5) = 3.0 \times 10^{-7} \text{ mbar}$ ). On the right side the material and the topographic contrast are highlighted.

exit area, the  $\text{SE}_{\text{I}}$ s contribute to the high resolution of the SEM images, while the  $\text{SE}_{\text{II}}$ s cause the background signal. The size of the interaction volume and therefore the area and the volume from which electrons and X-rays are emitted, depends on the sample material and the  $E_{\text{PE}}$ , and may extend to the  $\mu\text{m}$  range. As a general trend, it increases with increasing  $E_{\text{PE}}$ , decreasing atomic number ( $Z$ ) and density ( $\rho$ ). [16]

For the interpretation of SEM images, it is crucial to understand the different contrast mechanisms which may occur. In general, it has to be distinguished between *material* and *topographic contrast*. While the so-called material contrast reflects the chemical and physical properties (e.g.  $Z$ ,  $\rho$ , crystal orientation, magnetic properties, etc.), the topographic contrast is basically due to the morphology and the topography of the sample (roughness, edges, kinks, surface tilt, etc.).

An important material contrast is the *chemical contrast*, which is based on the locally differing number of BSEs. The higher  $Z$  and  $\rho$  of the irradiated material, the higher the BSE coefficient, i.e. the more BSEs are emitted. This contrast mechanism causes e.g. a brighter appearance of a metal in SEM compared to an area which is covered e.g. with carbon (cf. Figure 2.1). All SEM images in the work at hand were acquired using the SEs. This detection mode is dominated by topographic contrasts. However, as  $\text{SE}_{\text{II}}$ s originate from BSEs, the micrographs also have a superimposed chemical contrast.

On the other hand topographic contrasts like the so-called *surface-tilt contrast* and the *edge effect* are also important for the SEM images shown in this thesis. The origin of

these contrast mechanisms is an increased SE and BSE coefficient at edges and on surfaces which are inclined towards the impinging PE beam, i.e. these surface areas appear brighter in the SEM images.

In contrast to most SEMs which work in a high vacuum (HV) environment, for all experiments in this thesis a UHV-SEM was applied. The main advantage of UHV as compared to HV is a lower background pressure (typically in the low  $10^{-10}$  mbar regime), i.e. strongly reduced residual gases, which are mainly hydrocarbons in typical HV-instruments. Therefore, the well-known “black staining” of scanned areas, which is due to a deposition of hydrocarbons from the residual gases induced by the impinging PE beam, is usually not observed or at least strongly reduced when acquiring SEM images in UHV.

### **2.2. Auger electron spectroscopy (AES)**

Auger electron spectroscopy (AES) is a widespread surface science technique for analyzing the chemical composition of a sample. Upon interaction of e.g. an electron beam with the sample, AEs are emitted. The kinetic energy of these electrons is characteristic for the respective elements of the sample, and is independent of the excitation energy. It is typically between 50 and 2000 eV; due to the short inelastic mean free path of these electrons, AES is surface sensitive. The use of a focused electron beam opens up the possibility to perform local AES, AE line scans and scanning Auger electron microscopy (SAM). This is of particular importance as it enables to target the chemical analysis of individual nanostructures.

The so-called Auger effect, i.e. the emission of AEs, was discovered independently by Lise Meitner (1922) [17] and Pierre Auger (1923) [18]; it comprises three steps. In the first step, a core electron (e.g. from  $L_{2,3}$  shell) is emitted due to the excitation by a PE. In a second step, the generated core hole is refilled immediately by an outer shell electron (e.g.  $M_{2,3}$  shell). In a simplified picture, the energy which is released upon this intra-atomic electron transfer corresponds to the difference in orbital energies of the involved electrons. In a third step, this energy is transferred radiationless to another electron which is emitted as the so-called AE (e.g. from  $M_{4,5}$  shell). Another channel for relaxation is the emission of a photon (characteristic X-rays); these two processes are complementary. [18] The probability for the respective process is dependent on  $Z$  and the shell with the initial vacancy. For  $K$  shell vacancies, the AE relaxation process is prevailing up to  $Z = 15$ , while X-ray emission is negligible. [19] For the  $L$  and  $M$  shell vacancies a similar behavior is observed, however shifted to higher  $Z$  (to  $Z = 50$ ). [20] Therefore, if AES is compared to energy dispersive X-ray (EDX) analysis, one should keep in mind, that not only AES is

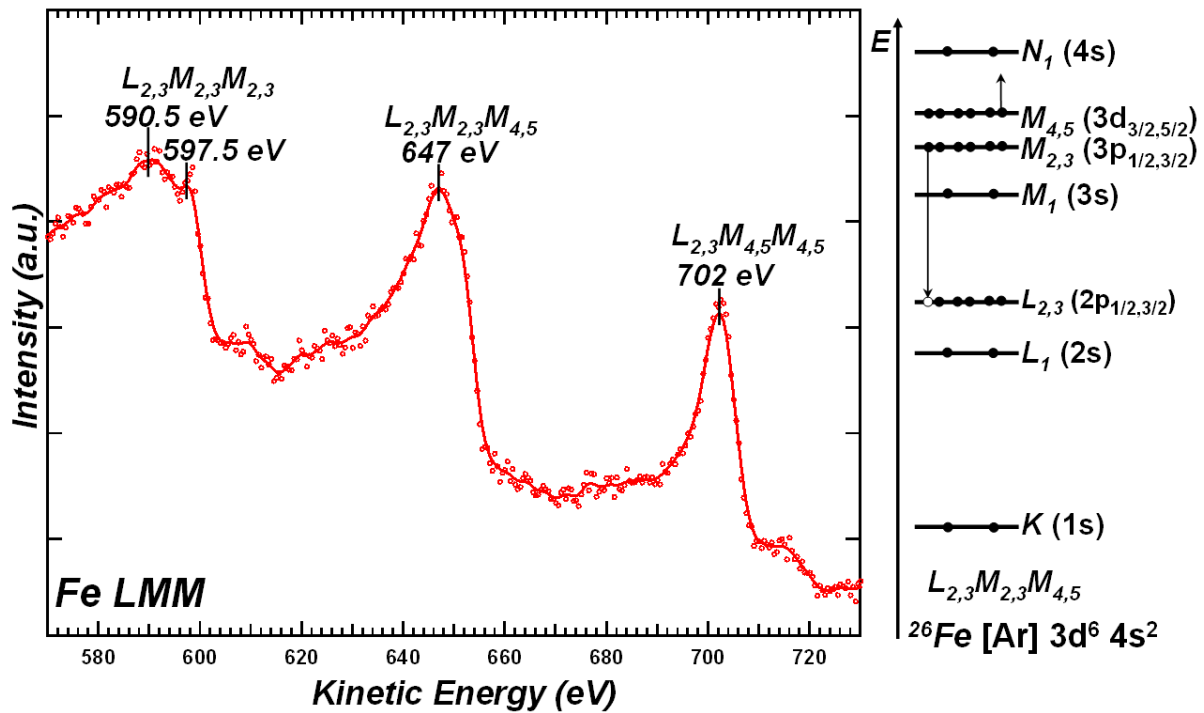


Figure 2.2 AE spectrum acquired on an Fe nanostructure deposited via EBID and autocatalytic growth on ultra-thin  $\text{SiO}_x$  on  $\text{Si}(001)$ .

more surface sensitive than EDX, but also that these processes have different element specific sensitivities. Based on these considerations it might be, that e.g. the carbon amount is overestimated with AES compared to an EDX analysis, as carbon contaminations are often located at the top-most surface layers (AES surface sensitive) and the C KLL transition is evaluated (higher AE decay probability,  $Z = 6$ ).

The kinetic energy of the Auger electron can be roughly approximated by the equation  $E_{L_{2,3}M_{2,3}M_{4,5}} = E_{L_{2,3}} - E_{M_{2,3}} - E_{M_{4,5}} - \Phi$ , with  $E_{L_{2,3}}$ ,  $E_{M_{2,3}}$ ,  $E_{M_{4,5}}$  being the electron binding energies of the involved shells and  $\Phi = E_{vac} - E_{Fermi}$  being the work function of the material. [21] This equation does not take into account the interaction energies between the holes ( $M_{2,3}$  and  $M_{4,5}$ ) in the final atomic state, and it also neglects the inter- and extra- atomic relaxation energies. The spectroscopic notation of the above described Auger transition is  $L_{2,3}M_{2,3}M_{4,5}$ . The first letter designates the shell containing the initial vacancy and the last two letters designate the shells containing electron vacancies left by the sequential relaxation. [22] In Figure 2.2 an AE spectrum of LMM transitions is depicted for the element Fe. Each of the LMM peaks can be assigned to a combination of an initial core hole in the  $L_{2,3}$  shell and to the successive electron transfer and emission from the two other involved shells,  $M_{2,3}$  and  $M_{4,5}$ ; this explains the different energy positions for the

*LMM* transitions. On the right side of the spectrum, the  $L_{2,3}M_{2,3}M_{4,5}$  transition is schematically depicted. As the kinetic energy of the AE is related to the energy levels of the involved shells, an AE spectrum reflects the chemical composition of the emitter. In addition, an AE spectrum contains information on the chemical binding states of the atoms. This so-called chemical shift reflects a redistribution of the electron density of states in the valence region induced by a specific chemical environment. This may result in a change in binding energies, which in turn leads to a change of the Auger peak position and / or the peak shape. [21]

AE spectra are usually acquired in the derivative mode  $dN(E)/dE$ ; however, for this work non-derivative spectra were recorded due to the excellent signal to noise ratio achievable in the applied set-up. The peak area of the AE peak is directly proportional to the number of emitted AEs. Quantitative evaluation, such as film thickness determination or compositional analysis, was performed by means of reference measurements. [23]

### **2.3. Quadrupole mass spectrometry (QMS)**

With a quadrupole mass spectrometer (QMS) the chemical composition of volatile molecules can be analyzed by ionizing the molecules and subsequent detection of the molecular ion or charged fragments. In this work, the QMS was utilized in particular for the analysis of the precursor  $\text{Fe}(\text{CO})_5$ .

For the QMS measurement three basic components are required, i.e. an ion source, a mass analyzer and a detector. The generation of the cations is performed by means of electron impact (EI) ionization. The mass analyzer, i.e. quadrupole rods, realizes, via a certain high-frequency alternating electrical field, which is superimposed on a direct current (DC) voltage, the separation of the mass-to-charge ( $m/z$ ) ratios. At a specific voltage ratio a certain  $m/z$  ratio oscillates through the rod system and will reach the detector. The other  $m/z$  ratios have instable trajectories and thus will not be detected. For the detection of the ions, a channeltron (channel electron multiplier, CEM) is used. [24] In this set-up the utilized QMS detects up to  $m/z = 200$ .

In general, in a QM spectrum the ion intensity is measured as a function of the  $m/z$  ratio. A typical spectrum of the precursor molecule  $\text{Fe}(\text{CO})_5$  is depicted in *Figure 2.3*. Dominant peaks arise at  $m/z = 28, 56, 84, 112, 140, 168, 196$ , which can be assigned to the fragments  $\text{CO}^+, \text{Fe}^+, \text{Fe}(\text{CO})^+, \text{Fe}(\text{CO})_2^+, \text{Fe}(\text{CO})_3^+, \text{Fe}(\text{CO})_4^+$  and the cation  $\text{Fe}(\text{CO})_5^+$  of the precursor molecule.

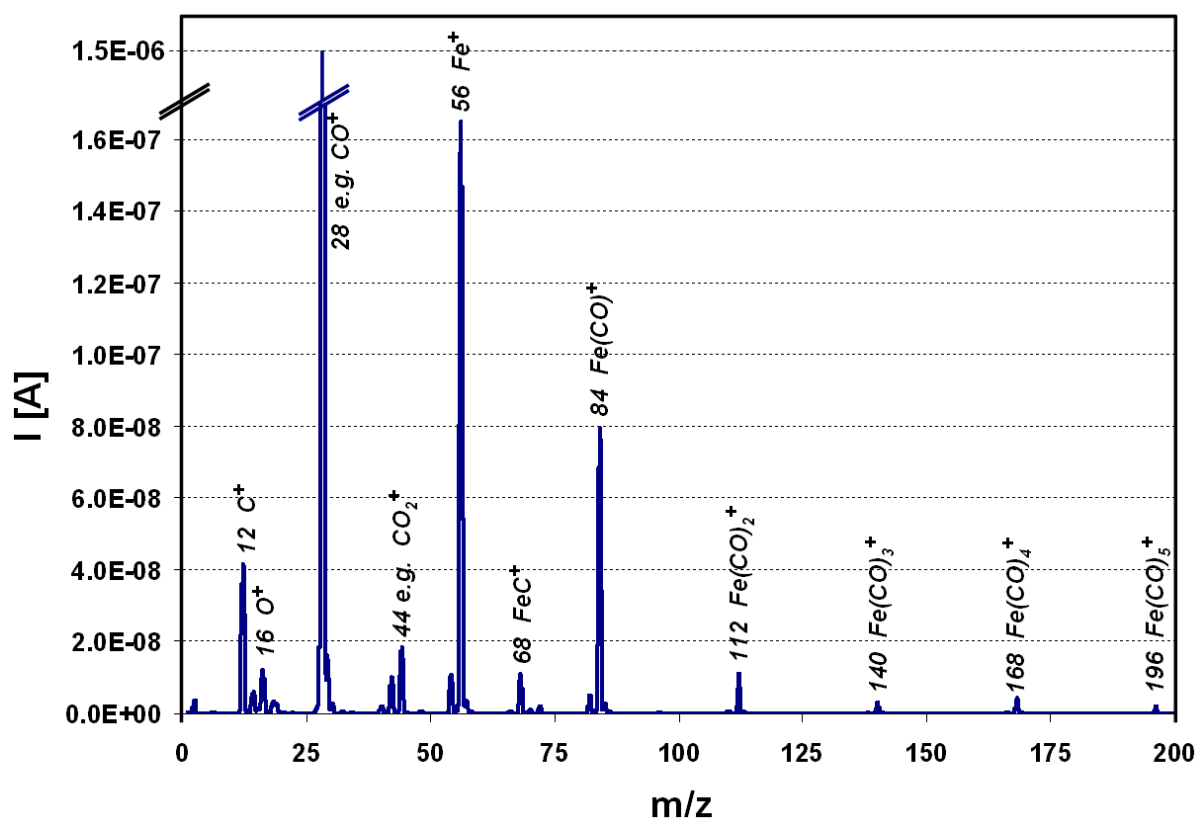


Figure 2.3 QM spectrum of  $\text{Fe}(\text{CO})_5$  acquired at a nominal background pressure of  $3.0 \times 10^{-7}$  mbar.

#### 2.4. Low energy electron diffraction (LEED)

Low energy electron diffraction (LEED) is a surface science technique which exploits the diffraction of low energy electrons to characterize the long range order of crystalline surfaces.

The de Broglie wavelength of the impinging electrons (typical energies 30 – 200 eV) is in the range of interatomic distances, which is decisive to fulfill the atomic diffraction condition. On a fluorescent screen the constructive interference of the scattered electrons can be observed as bright diffraction spots; this diffraction pattern is equivalent to the position of the reciprocal lattice rods intersecting the detection screen. Another consequence of using low energy electrons is that their inelastic mean free path in the sample is relatively short which results in a surface sensitive analysis of the specimen. [21]

For the work at hand, LEED was applied to analyze the long range atomic order of the sample surface. For this purpose the analysis and the judgment of the diffraction pattern's sharpness and spot geometry was necessary.

## **2.5. Electron beam induced lithographic techniques**

For this thesis two focused electron beam induced processing (FEBIP) techniques were applied. Both rely on a focused electron beam, which is utilized to cause chemical modification very locally, and on the molecule  $\text{Fe}(\text{CO})_5$  as precursor for the deposition of Fe.

### **2.5.1. Electron beam induced deposition (EBID)**

A key challenge when fabricating nanostructures is controlling their exact location and chemical composition. [25] One of the nanofabrication techniques, which addresses these challenges, is electron beam induced deposition (EBID). [26-28] Under the influence of a focused electron beam (e.g. from an SEM or a scanning transmission electron microscope (STEM)), the local dissociation of adsorbed precursor molecules is induced (cf. *Figure 2.4a-b*), and a deposit, composed of the non-volatile fragments of the precursor molecule, is formed (cf. *Figure 2.4c*). In a simple analogy, the electron beam might be regarded as a “pen” and the precursor molecules as “ink”.

Besides the molecule  $\text{Fe}(\text{CO})_5$ , in principle all volatile compounds bearing the targeted material can be utilized as precursor. In general, EBID is a direct writing method, which can be applied on plane and on non-planar substrates for the generation of two- and even three-dimensional structures [8]. A potential drawback is e.g. the rather low deposition rate [26]. Nonetheless, EBID recently has become the state-of-the-art technique to repair EUV lithographic masks in semiconductor industry. [29] Furthermore, it can be utilized for the fabrication of scanning probe sensors, for circuit editing (in combination with electron beam induced etching, EBIE) and for the generation of nanophotonics, micro- and nanoelectronics. [27]

The historic development of EBID is directly correlated to the fact that most SEMs work under high vacuum (HV). If a sample is scanned for imaging with the electron beam in such a set-up, a blackening of the surface is observed, which can be explained by the electron induced deposition of carbonaceous residual gases (e.g. hydrocarbons from pump oils), as observed already e.g. by Ennos et al. in 1953. [30] Such contamination growth might be even used on purpose, e.g. as negative resist for the fabrication of extremely small metal structures in an ion etching process. [31] The first reported use of EBID was by Barker and Morris in 1961. [32] Working under HV conditions, it is not surprising that often poor purities of the EBI deposits are observed, which may result from a co-deposition of residual gases. Another source for contamination is the dissociation of carbonaceous ligands from organometallic precursors.

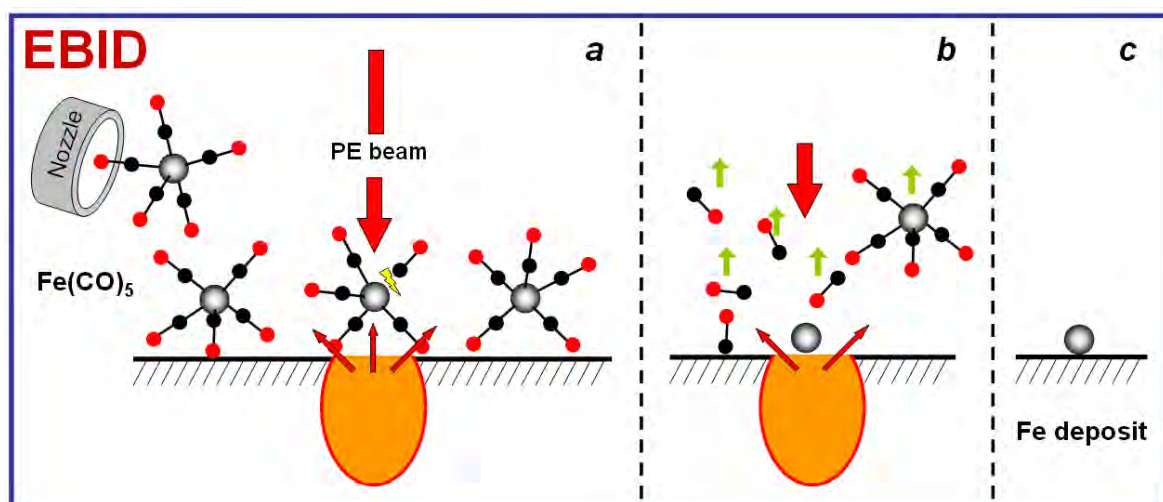


Figure 2.4 Scheme of the idealized EBID process: (a) irradiation of adsorbed  $\text{Fe}(\text{CO})_5$  with the focused electron beam; (b) dissociation of the precursor and desorption of volatile fragments; (c) deposition of non-volatile fragments.

Typical metal-contents of 15 to 60 % are reported, with the main contaminations being carbon and oxygen. [6-8] Applying a “surface science” approach, i.e. working under UHV, strongly decreases the background pressure reducing the co-deposition of carbonaceous residual gases significantly. Besides a lower contamination level of the deposits, in UHV also clean surfaces can be maintained on the time scale of typical EBID experiments.

Other approaches to reduce contaminations in the EBI deposit, like e.g. applying higher current densities [33, 34], heating during the EBID experiment [7, 35] or the use of inorganic precursors (without carbon containing ligands) [36, 37], have been successfully performed.

Electrons causing precursor dissociation are the impinging PEs (for all experiments in this thesis  $E_{PE} = 15 \text{ keV}$ ), the BSEs, the induced SEs and, as soon as a deposit is forming, also forward scattered electrons (FSEs). The scattering of electrons and the emission of SEs result in an effective broadening of processed area, which is referred to as proximity effects. In EBID, these are unintended deposits in the vicinity of the PE beam impact point. [26]

The two most important proximity effects for the work at hand, are the BSE and the FSE proximity effect, which are caused by the respective electrons and the thereby induced SEs. The BSE proximity effect is confined to the area from which BSEs are emitted (BSE exit area); this area can be approximated for high electron doses via a Monte Carlo simulation (e.g. with the program *Casino V2.42* [38]). Here, secondary

electrons (< 50 eV) are omitted; however, in particular these low energy electrons have high cross-sections for triggering chemical reactions. The FSE proximity effect can cause deposits even further away from the initial impact point as compared to the BSE proximity effect. Obstacles on the pathway of the FSEs might cause so-called shadowing effects, i.e. behind those obstacles no deposition occurs; the observation of this effect is a clear indication for the FSE proximity effect.

The involved electrons have a broad energy distribution, resulting in different dissociation mechanisms for the precursor, listed in the following, which were mainly measured in gas phase. However, EBID is performed on a surface, therefore the interplay with the solid may open up new pathways for relaxation and change the dissociation cross sections. [39, 40]

The high energy PEs, BSEs and FSEs may induce dissociation of the precursor via so-called dissociative ionization (DI) (having the highest cross section between 70 – 100 eV [27]). Another mechanism is the dissociation into neutrals, which has the highest cross section around 50 eV [27]. For low energy electrons, as the SEs, the so-called dissociative electron attachment (DEA, highest cross section around 15 eV [41]) and the dipolar dissociation (DD, highest cross section for only a few eV [42]) are the main pathways for precursor dissociation.

It is obvious that these dissociation mechanisms have their highest cross section at rather low energies, therefore one might conclude that mainly the SEs and low energy BSEs contribute to the dissociation. However, the current density of the PEs (considering a focused electron beam) is higher than for SEs ( $SE_{IIS} > SE_{IS}$ ) and BSEs (the current density of  $SE_{IIS}$  and BSEs is generally in the same order of magnitude). Therefore, although the cross section for the high energy PEs is the lowest, a significant contribution to the deposition might be due to the high current density.

The growth rate of an EBI deposit is a complex quantity, influenced by a variety of parameters. [28] They can be divided in experimental and system immanent parameters listed in *Table 2.1*; partially, they are dependent on each other, like e.g. temperature influences residence time, sticking probability and adsorption, desorption and diffusion rates.

Depending on these parameters, two main deposition regimes are observed, i.e. the so-called electron limited and the transport limited regime; the latter can be divided depending on the main pathway of the precursor supply, i.e. adsorption (in literature referred to as precursor limited regime [26]) and diffusion (in literature referred to

<b>Parameters determining the growth rate for a given substrate &amp; precursor</b>	
<b>Experimental</b>	<b>System immanent</b>
>> Beam energy	>> Energy distribution along BSE exit area
>> Beam current / current density (PEs)	>> Current density distribution (BSEs, FEs, SEs)
>> Pressure / Precursor flux	>> Residence time
>> Temperature	>> Sticking probability
>> Scanning parameters (dwell time, step size, replenishment time, pattern, etc.)	>> Adsorption, desorption, diffusion rates
>> Time	>> Nanostructure morphology
	>> Cross section

*Table 2.1 Experimental and system immanent parameters influencing the growth rate for a given substrate and precursor molecule.*

as diffusion-enhanced regime [27]). If there is an excess of electrons, the deposition is limited by the precursor; this is referred to as transport limited regime. If the situation is reversed, i.e. there are more precursors than can be dissociated by the electrons, it is referred to as electron limited regime. For the work at hand the different deposition regimes and also the EBID deposition rate certainly influence the deposit's shape; however, for  $\text{Fe}(\text{CO})_5$ , the autocatalytic growth properties of this precursor influence the final topography as well (cf. *Chapter 2.5.3*).

For more details on EBID the reader is referred to the reviews by van Dorp and Hagen [26], Utke et al. [27], Randolph et al. [28], Silvis-Cividjian and Hagen [43] and Botman et al. [7].

### **2.5.2. Electron beam induced surface activation (EBISA)**

Electron beam induced surface activation (EBISA) is a lithographic method, which is described for the first time in the framework of this thesis. In this chapter some results of this thesis are summarized to explain this novel technique. For more details the reader is referred to the results part (cf. *Chapter 3.1 & 3.2*).

This FEBIP technique employs a focused electron beam to locally modify a surface (cf. *Figure 2.5a*), in this thesis silicon oxide, such that upon  $\text{Fe}(\text{CO})_5$  dosage, the molecules dissociate at the generated active sites and Fe nuclei form (cf. *Figure 2.5b-c*) at room temperature (RT). These active sites are oxygen vacancies, i.e. SiO, which are locally generated by electron stimulated desorption (ESD) of oxygen, presumably via a Knotek – Feibelman mechanism. [44]

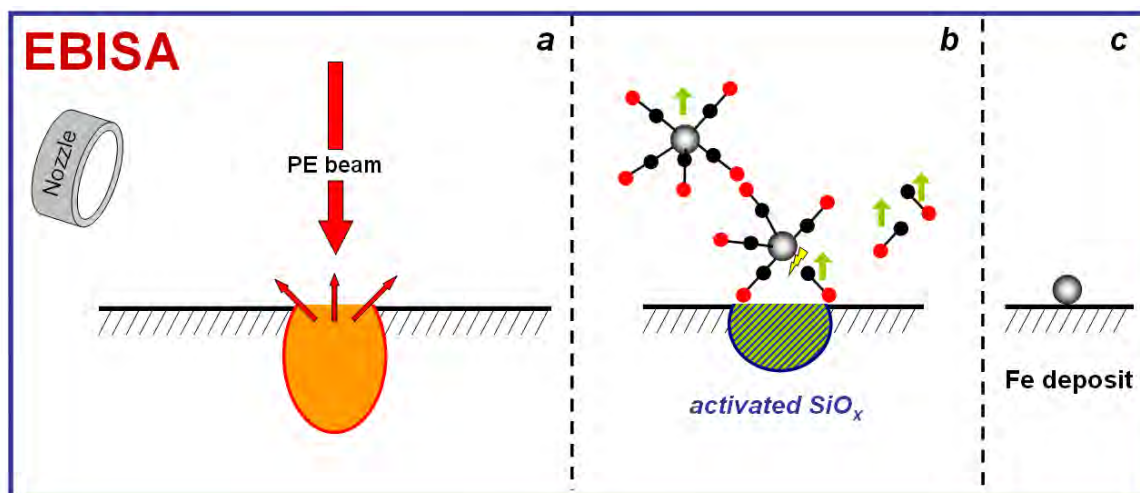
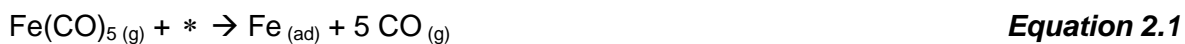


Figure 2.5 Scheme of the idealized EBISA process: (a) irradiation of the surface with a focused electron beam; (b) dosage of  $\text{Fe}(\text{CO})_5$ , adsorption and diffusion on the surface, dissociation at the activated sites; (c) formation of initial Fe nuclei.

As an analogy, the electrons may be imagined as “invisible ink”, which can be “developed” by the dosage of the precursor molecule.

The EBISA process might be described with the following simplified equation, regarding solely the initial and the final state. The asterisk \* refers to a free adsorption site on the activated  $\text{SiO}_x$ .



In the work at hand the EBISA process was studied with successive autocatalytic growth. Thereby, the applied precursor molecule  $\text{Fe}(\text{CO})_5$  autocatalytically decomposes on initial Fe deposits (cf. Chapter 2.5.3, Figure 2.6), resulting in additional growth upon prolonged precursor dosage. This can be regarded as a parallel processing step. Thus, the top-down EBISA process followed by the bottom-up autocatalytic growth, allows for the local fabrication of a solid deposit on a surface.

Since no deposit forms during electron irradiation (base pressure  $< 1 \times 10^{-10}$  mbar), no forward scattering of PEs occurs. Thus, the FSE proximity effect, which does affect EBID, does not play a role here. However, the PEs are still backscattered, therefore the BSE proximity effect is observed. By choosing the correct electron dose ( $\leq 2 \mu\text{C}/\text{cm}$ ) and additional gas dosage time (AGDT), this proximity effect can be severely diminished or even completely suppressed. On surface areas activated with such low electron doses, the initial dissociation of  $\text{Fe}(\text{CO})_5$  at the very locally generated defect sites can be used for the deposition of significant amounts of material by means of autocatalytic growth, thus without suffering from FSE and BSE proximity effects at all. Therefore, much more

## 2. Fundamentals & techniques

---

material can be locally deposited via EBISA compared to EBID without unintended deposition in close vicinity. The mostly autocatalytic decomposition in UHV at RT is interpreted as being the reason for the very high purity of the deposits. It should be mentioned that the generated active sites and the autocatalytic dissociation behavior of  $\text{Fe}(\text{CO})_5$  are sensitive towards impurities on the surface, which might be explained by a blocking of active sites. Therefore, providing clean samples and maintaining them in UHV might be even more important for EBISA than for EBID.

### 2.5.3. Autocatalytic growth

In the previous chapters (EBID & EBISA) it was mentioned that the precursor  $\text{Fe}(\text{CO})_5$  exhibits autocatalytic growth properties, which lead to an additional growth at the initial iron deposit upon prolonged gas dosage. Therefore, in this chapter the autocatalytic growth properties of  $\text{Fe}(\text{CO})_5$  are discussed (cf. *Figure 2.6*).

Autocatalysis is a process in which one of the reaction products catalyzes the reaction itself. The autocatalytic dissociation of the iron pentacarbonyl molecule can be described with the following, again, strongly simplified equation, omitting all intermediate states.



In literature the autocatalytic growth behavior of  $\text{Fe}(\text{CO})_5$  is reported by several research groups. In the following a brief overview of selected results is given.

Kunz et al. demonstrated that  $\text{Fe}(\text{CO})_5$  autocatalytically decomposes on already deposited EBID iron structures on silicon at elevated temperatures, i.e. at  $\sim 400$  K (this process is referred to as selective area deposition). High EBID rates were observed, which were explained by autocatalytic growth rate enhancement during the deposition process. [45-47] Such thermally assisted autocatalytic growth of  $\text{Fe}(\text{CO})_5$  was also observed by Hochleitner et al.; here, fast growth rates of tip deposits on native silicon oxide on Si were attributed to electron beam induced heating (EBIH) from beam current dependent measurements. [48]

Besides Fe as dissociation site for  $\text{Fe}(\text{CO})_5$  at elevated temperatures, also defect sites were exploited for selective area deposition. The bombardment of a Si sample (native oxide removed) with  $\text{Ga}^+$  ions and successive  $\text{Fe}(\text{CO})_5$  dosage at a substrate temperature of  $\sim 400$  K led to selective Fe deposition in the pre-irradiated regions. Interestingly, deposition was only observed for ion doses of  $\sim 4 \times 10^{11} \text{ Ga}^+/\text{cm}$ . At an order of magnitude higher or lower ion doses, no growth was observed. [49]

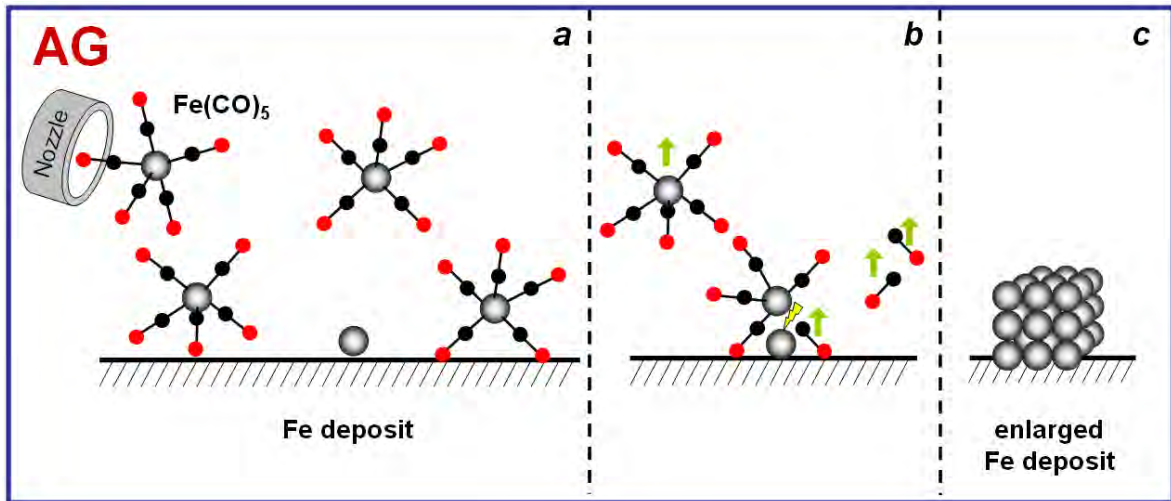


Figure 2.6 Scheme of the idealized autocatalytic growth (AG) process: (a) dosage of  $\text{Fe}(\text{CO})_5$  on initial EBID or EBISA Fe nuclei; (b) autocatalytic dissociation of  $\text{Fe}(\text{CO})_5$ ; (c) enlarged, final Fe deposit.

Note that all investigations, which have been mentioned so far, were performed under HV conditions. In UHV, for example, Adams et al. showed that hydrogen passivated Si(100) in combination with  $\text{Fe}(\text{CO})_5$  can be utilized for selective area deposition: the monohydride resist is locally removed with a scanning tunneling microscope (STM) tip (ESD of H), successive exposure to  $\text{Fe}(\text{CO})_5$  at  $\sim 550$  K results in local deposition of Fe at the Si dangling bond sites. [50, 51]

All of these studies have in common that they are based on autocatalytic decomposition of  $\text{Fe}(\text{CO})_5$  above room temperature. The Fe content which was often around 80 – 85 % in the reported works [48, 49] is exceeded in the experiments discussed in this thesis. The higher contamination levels (basically C and O) of autocatalytically grown Fe at elevated temperatures might be interpreted as being due to a dissociative chemisorption of the CO ligands on Fe, which sets in at RT (300 K). [52-56] This suggests that, although higher growth rates are observed at elevated temperatures, the generated deposits suffer from a lower purity. In addition, also the HV conditions, i.e. more residual gases, might result in an incorporation of carbonaceous residues during the autocatalytic growth.

For UHV, it was shown that the autocatalytic growth behavior can be employed already at RT, which was also exploited in the work at hand. Lukasczyk et al. observed the catalytic decomposition of  $\text{Fe}(\text{CO})_5$  on a Rh(110) surface and the successive autocatalytic growth upon prolonged gas dosage at RT. [71] Zaera noticed on Pt(111) that at temperatures as low as 280 K a steady Fe film growth from  $\text{Fe}(\text{CO})_5$  is observed. [52] That the autocatalytic growth is observed at RT under UHV, but not under HV conditions, might be explained e.g. by blocking of adsorption sites for  $\text{Fe}(\text{CO})_5$ .

## 2. Fundamentals & techniques

---

Applying a precursor like  $\text{Fe}(\text{CO})_5$ , it is obvious that parameters like the AGDT, the temperature and the precursor flux (pressure) might affect the deposited amount as well as the morphology of the deposit. In general, it can be stated that the longer the AGDT [57], the higher temperature [52, 58, 59] and pressure [48], the more material is deposited. For the latter there are also reports on a “negative pressure dependence”: Zaera observed that e.g. on Pt(111) at 280 K an increase of the pressure from  $2.7 \times 10^{-8}$  to  $2.7 \times 10^{-7}$  mbar, decreased the growth rate by a factor of about 2.7, which was explained by blocking of active sites by co-adsorbed CO. [52]

### 2.5.4. Lithographic control

To perform lithography, the position of the electron beam has to be controlled. For this purpose two set-ups were applied. In the beginning of the work arbitrary waveform generators (ARBs, Hewlett Packard 33120A), then later a LabVIEW-based (LabVIEW 8.6, National Instruments) beam control attachment was utilized. The external scan input terminal of the Zeiss system allows for beam control of the SEM via +/- 10 V signals, in x and y direction. The ARBs and the LabVIEW-based control differ in sampling rate (40 MHz vs. 60 MHz) and in the digital-to-analog converter (DAC) resolution (12 Bit vs. 14 Bit). The deflection of the electron beam induced by the +/- 10 V signal is directly correlated to the magnification in the SEM. The minimum step size is given by the amplitude resolution (DAC resolution), while the minimum dwell time of the electron beam is determined by the sampling rate. Therefore, the LabVIEW based beam control has the advantage of smaller achievable step sizes and shorter dwell times compared to the ARB based control. Moreover, the LabVIEW based beam control allows for the generation of more complex patterns (128 MSamples compared to 16 kSamples of memory) than the ARBs, for implementing beam blanking commands and for interfacing with the piezo stage for sample positioning.

In this thesis, mainly point and line irradiation were applied for the fabrication of deposits. For point irradiation the spot mode of the SEM Zeiss software was utilized; the applied electron dose was adjusted by time of irradiation (electron dose  $d = t I_{PE}$ ). For line irradiation the magnification was set to 2445 ( $46.76 \mu\text{m} \times 35.07 \mu\text{m}$ ) when using the LabVIEW based software, and to 1000 ( $114.3 \mu\text{m} \times 85.75 \mu\text{m}$ ) when using the ARBs. For both the length of the irradiated line was set to  $45 \mu\text{m}$  and the step size (ss) to 12 nm. Multiple and one sweep (ms and os) lines have been investigated. For ms lines the dwell time ( $t_{dw}$ ) was 80 ns resulting in an active line scan time of 300  $\mu\text{s}$ . The waiting time after each line was 500  $\mu\text{s}$ . The electron dose of the ms lines was adjusted via the number of

sweeps ( $n$ ). For the os lines ( $n = 1$ ) the electron dose was adjusted via the dwell time. For both the electron line dose is  $d = (t_{dw} I_{PE} n)/SS$ .

## 2.6. Investigated surfaces & precursor molecule

### 2.6.1. Silicon oxide on silicon and silicon nitride

The EBID and EBISA process followed by successive autocatalytic growth was studied on different substrate types. In general, all of them have in common that they are silicon based specimens. The interface is in all cases a silicon oxide, which is either a thermal or a native silicon oxide. This silicon oxide is supported by silicon (Si) and / or by silicon nitride (SiN). Besides these variations, also the influence of the substrate thickness on electron scattering processes was investigated, i.e. bulk samples were compared to membranes. An overview of all applied samples with the used abbreviations is given in *Table 2.2*.

The 300 nm SiO<sub>x</sub> was purchased with a protective coating consisting of a mixture of n-butyl acetate and cyclohexanone-formaldehyde resin (Illmar P4), which can be removed via sonication in acetone. The ultra-thin SiO<sub>x</sub> has been prepared by thermal oxidation of a flashed Si(001) specimen *in situ* in the UHV chamber. The Si-bulk sample is such a Si(001) sample but without flashing, i.e. the native SiO<sub>x</sub> layer is intact. All SiN based samples have been used with their native SiO<sub>x</sub> as well. These samples have been purchased without protective coating. The thickness of the native SiO<sub>x</sub> film was determined to be ~ 1.3 nm on the Si-bulk and ~ 1.1 nm on the SiN-bulk sample via AES measurements.

SiO <sub>x</sub> type	Abbreviation	Substrate	Composition
Thermal	300 nm SiO <sub>x</sub>	Si	300 nm SiO <sub>x</sub> (thermal) on Si(001)
	ultra-thin SiO <sub>x</sub>		~ 0.5 nm SiO <sub>x</sub> (thermal) on Si(001)
Native	Si-bulk	SiN / Si	SiO <sub>x</sub> (nat.) on Si(001)
	SiN-bulk		SiO <sub>x</sub> (nat.) / 50 nm SiN / Si
	SiN-50nm	SiN	SiO <sub>x</sub> (nat.) / 50 nm SiN-membrane
	SiN-200nm		SiO <sub>x</sub> (nat.) / 200 nm SiN-membrane

*Table 2.2 List of substrate types which have been applied for the experiments.*

### 2.6.2. Iron pentacarbonyl ( $\text{Fe}(\text{CO})_5$ )

The precursor iron pentacarbonyl,  $\text{Fe}(\text{CO})_5$  (color: yellow to amber, density  $1.49 \text{ g/cm}^3$  at 298 K), which belongs to the category of metal carbonyls  $\text{M}_n(\text{CO})_m$ , is chosen for the deposition of iron via electron induced processes for two main reasons:

(1) The ligand carbon monoxide, CO, has a high dissociation energy of about 11.1 eV [60, 61]; in contrast, the dissociation energies of the Fe-CO bonds are in the order of 1 - 2 eV [62, 63] (note that the exact dissociation energy depends on the total number of COs attached to the Fe). These energies suggest that the Fe-CO bond dissociates more readily upon electron bombardment than the CO itself. Still, the electron induced dissociation of CO is observed. [64] However, besides the latter process, there is also the ESD which might become prevailing upon electron irradiation. On Ir(111), it was e.g. shown that the electron induced dissociation of CO occurs only at 1 – 2 % of the rate of the ESD. [65] If intact, CO is readily volatile, e.g. on Si and  $\text{SiO}_x$ , and therefore a good leaving group upon molecule dissociation. In addition, CO has the lowest possible carbon amount incorporated compared to any other organic ligand, which reduces the potential carbon content in the iron deposit.

(2)  $\text{Fe}(\text{CO})_5$  is easily volatile with a vapor pressure of  $\sim 47 \text{ mbar}$  at 298 K [66], which suits it well for gas dosage.

Besides these reasons, for which  $\text{Fe}(\text{CO})_5$  is considered to be an appropriate precursor molecule, it has the drawback that it is a toxic liquid and is air sensitive; thus, it must be handled with care and stored under inert gas.

### 2.7. UHV instrument

The main parts of the UHV system are the preparation and the analysis chamber, a fast entry lock (FEL) and a self-constructed gas dosage system. The system (cf. *Figure 2.7*) was purchased from Omicron Nanotechnology GmbH. The set-up is vibration damped via a passive vibration isolation system. The UHV instrument will be briefly described in the following; for further details the reader is referred to [13] and [23].

The preparation chamber is equipped with a QMS (Prisma QME 200, Pfeiffer), LEED optics (Spectraleed, Omicron), a quartz crystal micro balance (OSC-100A, Syscon), an electron beam evaporator (EFM 3i, Focus), a sputter gun (ISE 10, Omicron) and leak valves. The FEL is mounted on the preparation chamber and allows for fast introduction of samples without breaking the vacuum. The manipulator in the preparation chamber is equipped with a heating and cooling system and temperature readout. For the work at hand solely heating of Si samples was performed. This is realized by direct current

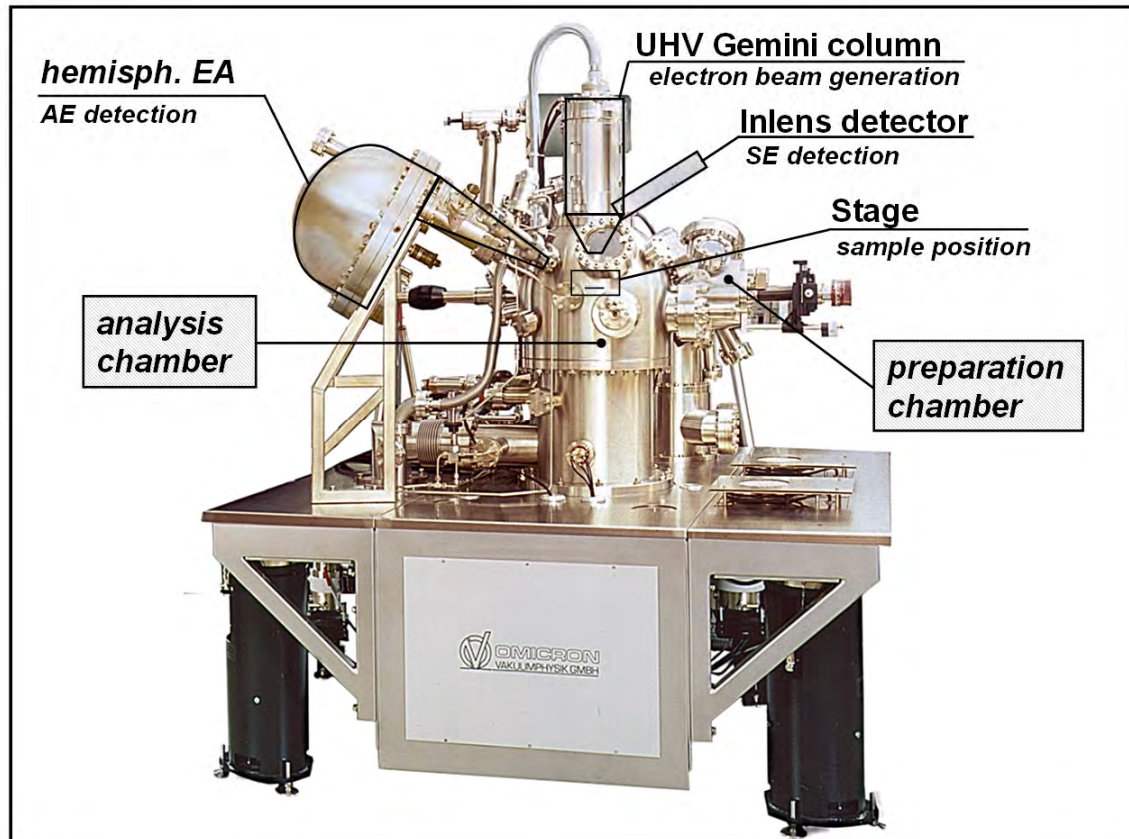


Figure 2.7 Image of the UHV system without cables, gas dosage system and dosing nozzle. The main parts of the analysis chamber are highlighted.

resistive heating of the sample itself. For temperature readout a pyrometer was used.

The analysis chamber is equipped with an electron column (UHV Gemini column, Zeiss), an Inlens and external SE detector, a hemispherical energy analyzer (NanoSAM EA U7 analyzer, Omicron), an STM (Omicron), a QMS (Prisma QME 200, Pfeiffer), a sample storage carousel (double-deck, 12 samples) and a wobble stick (FERROVAC). The position of the sample stage can be adjusted via piezoelectric inertia drive elements. A position readout system enables the re-positioning of the stage with a deviation less than  $2\ \mu\text{m}$  (even for maximum displacement of  $10 \times 10\ \text{mm}$  [67] in sample position). The gas dosage system is connected to the analysis chamber; via leak valves and a subsequent dosing nozzle gases can be introduced. The distance of the dosing nozzle ending (inner diameter 3 mm) to the sample can be adjusted via a linear transfer system. For this thesis the distance was adjusted to  $\sim 12\ \text{mm}$  leading to an estimated local  $\text{Fe}(\text{CO})_5$  pressure at the surface, which is enhanced by a factor of  $\sim 30$  ( $9.0 \times 10^{-6}\ \text{mbar}$ ) as compared to the nominal background pressure of  $3.0 \times 10^{-7}\ \text{mbar}$  which was adjusted for all deposition experiments. The gas dosage system is a separate UHV chamber, which is equipped with a QMS (Prisma QME 200, Pfeiffer) for precursor monitoring.

Two electron beam operation modi were applied, i.e.  $I_{PE} = 400\ \text{pA}$  (SEM / EBID /

## 2. Fundamentals & techniques

---

EBISA) and  $I_{PE} = 3$  nA (AES / SAM), both at  $U_{PE} = 15$  kV. The electron beam diameter for these modi is  $\sim 3$  nm and  $\sim 6$  nm, respectively, determined with a 20-to-80 criterion using a Au on C sample. [68]

## 3. Results

The fabrication of conductive nanostructures on an insulating material is of pivotal interest for electronic applications. As a prototype example for such a material combination, clean iron nanostructures on silicon oxide are investigated. For this purpose, electron beam induced deposition (EBID) followed by successive autocatalytic growth was performed with the precursor iron pentacarbonyl,  $\text{Fe}(\text{CO})_5$ , on 300 nm  $\text{SiO}_x$  on Si(001) at room temperature (RT). From this starting point, the new lithographic method electron beam induced surface activation (EBISA) was discovered and explored (*Chapter 3.1*). Using *in situ* prepared ultra-thin  $\text{SiO}_x$  on Si(001) substrates the mechanistic understanding of this novel process was deepened (*Chapter 3.2*). In addition to these investigations on thermal silicon oxides, the concept of EBISA was also transferred to native silicon oxide on silicon and on silicon nitrides (SiN). In a combining study of the two latter substrates in comparison to SiN-membranes, proximity effects were studied for EBISA and EBID (*Chapter 3.3*). In *Chapters 3.4* and *3.5*, the physical and chemical properties of the generated iron structures are highlighted, which were subject to cooperations with the Goethe University Frankfurt (Prof. Dr. Michael Huth) and the Technical University Vienna (Ass.-Prof. Dr. Alois Lugstein), respectively. In *Chapter 3.4*, besides the electrical- and magnetotransport measurements, the phenomenon of the inhibition of autocatalytic growth is also discussed. In *Chapter 3.5*, the growth of Si nanowires on EBISA Fe nanostructures as catalyst is reported.

### 3.1. Local pre-activation with electrons [P1]

In this chapter, the deposition of Fe on the industrial standard 300 nm  $\text{SiO}_x$  on Si(001) by means of FEBIP at RT is summarized. As a representative example an EBID line deposit realized with an electron dose of  $1.9 \mu\text{C}/\text{cm}$  is discussed, which is observed in the SEM as a dark staining of the oxidic surface (cf. *Figure 3.1*). Interestingly, with increasing additional gas dosage time (AGDT) after EBID more material is deposited. The morphology of the line deposit in SEM changes from a darkened surface (AGDT = 0 min) to a granular (AGDT = 15 – 105 min) and then to a polycubic (AGDT = 120 – 180 min) bright nanowire. The additional growth upon AGDT is interpreted as being due to autocatalytic dissociation of  $\text{Fe}(\text{CO})_5$  at initially deposited Fe nuclei. The scattered features in proximity of the line structure, which increase with AGDT, are attributed to the BSE proximity effect. The diameter of the central line deposit increases linearly with AGDT from about 30 nm (15 min, cf. *Figure 3.1*) to about 90 nm (180 min); this

### 3. Results

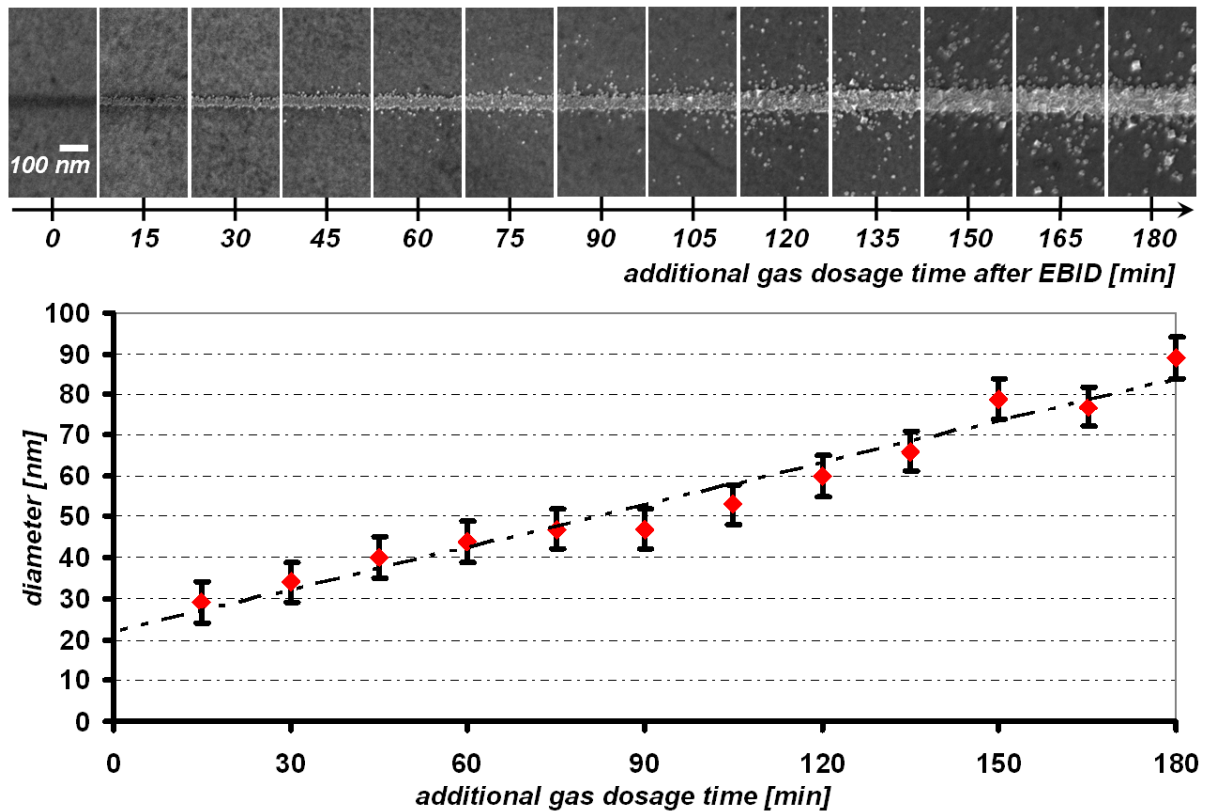


Figure 3.1 SEM images of EBID Fe line deposits ( $1.9 \mu\text{C}/\text{cm}$ ,  $300 \text{ nm SiO}_x$  on  $\text{Si}(001)$ ) with varying AGDT (0 – 180 min) at  $p(\text{Fe}(\text{CO})_5) = 3.0 \times 10^{-7} \text{ mbar}$  after the EBID process. Below, diameter evaluation of the lines vs. the AGDT.

corresponds to a lateral growth rate of  $\sim 0.2 \text{ nm}/\text{min}$  to both sides of the line. The average height of the line structures was measured with an *ex situ* atomic force microscope (AFM) for the line structures with an AGDT of 150 – 180 min and increases linearly from  $\sim 20$  to  $\sim 23$  to  $\sim 26 \text{ nm}$ , which is equal to a height growth rate of  $\sim 0.2 \text{ nm}/\text{min}$ ; this means that the lateral and the vertical growth rate are equal, leading to an overall deposition rate of  $\sim 3.3 \times 10^{-3} \text{ ML} / \text{L}$ . This is in excellent agreement with previous reports. [52]

In addition to the AGDT, the amount of the initially deposited Fe nuclei influences the size and morphology of the autocatalytically grown deposit. In Figure 3.2 EBID line structures fabricated with  $0.5 - 8 \mu\text{C}/\text{cm}$  and successive autocatalytic growth are depicted. While the BSE proximity effect is suppressed for  $0.5 \mu\text{C}/\text{cm}$  (line diameter  $\sim 100 \text{ nm}$ ), it increases with electron dose (for  $8 \mu\text{C}/\text{cm} \sim 3600 \text{ nm}$ ). The maximum diameter of the line structure is limited by the BSE exit area, if no significant height growth occurs during the EBID. The polycubic substructure of the autocatalytically grown deposit for higher AGDTs is in line with the growth of pure bcc  $\alpha$ -iron crystals. This assumption is supported by local AES, which indicates an Fe content higher than 95 %, contaminants being carbon and oxygen. The deposited Fe on the  $\text{SiO}_x$  sample is expected to have a brighter appearance

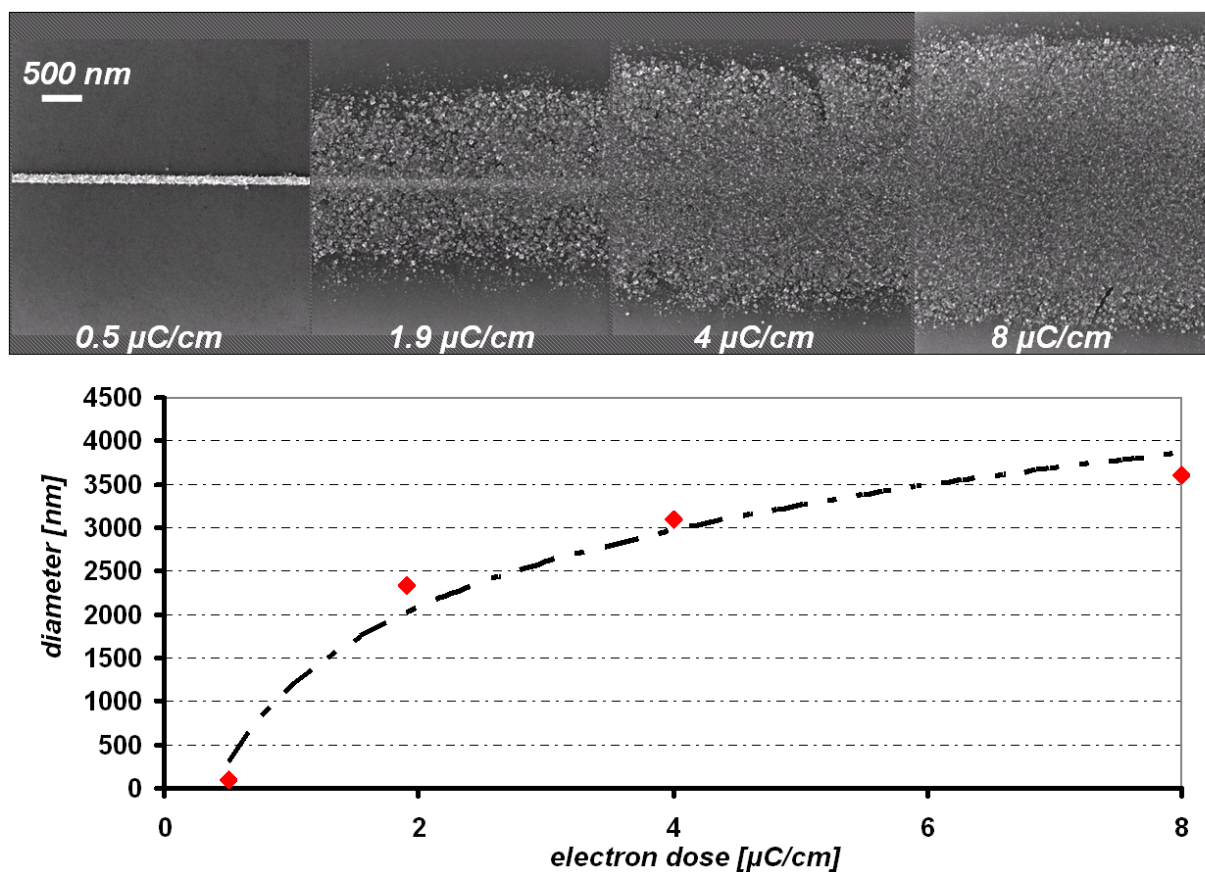


Figure 3.2 SEM images of Fe nano- to microwires fabricated on 300 nm  $\text{SiO}_x$  on  $\text{Si}(001)$  via EBID ( $0.5 - 8 \mu\text{C}/\text{cm}$ ) and an AGDT of approx. 250 min at  $p(\text{Fe}(\text{CO})_5) = 3.0 \times 10^{-7}$  mbar. Below, evaluation of the diameter vs. the applied electron line dose.

in SEM than the substrate due to the higher  $Z$  [16], which is indeed observed for high AGDT (cf. Chapter 2.1, Figure 2.1). The amount of initially deposited Fe nuclei (at AGDT = 0 min) must be therefore very low, as solely a dark staining of the surface is observed (cf. Figure 3.1). Furthermore, this darkening of the 300 nm  $\text{SiO}_x$  is also observed upon acquisition of standard SEM images, therefore one might suspect that the  $\text{SiO}_x$  substrate is locally modified by the electron beam irradiation such that the dissociation of the  $\text{Fe}(\text{CO})_5$  is promoted.

To test this hypothesis, in a first step the surface was irradiated with the electron beam under UHV conditions, and then in a second step  $\text{Fe}(\text{CO})_5$  was dosed for a certain time. Figure 3.3 shows SEM images of line deposits with increasing electron dose, which demonstrate that the precursor dissociates indeed at these pre-irradiated areas. The resulting Fe nuclei serve then as seed for further autocatalytic growth at RT. Those two steps, the local alteration of the surface and the subsequent exposure of the “activated” surface to  $\text{Fe}(\text{CO})_5$ , represent an alternative to EBID for the local deposition of material. This FEBIP lithographic technique, which is reported for the first time in the framework

### 3. Results

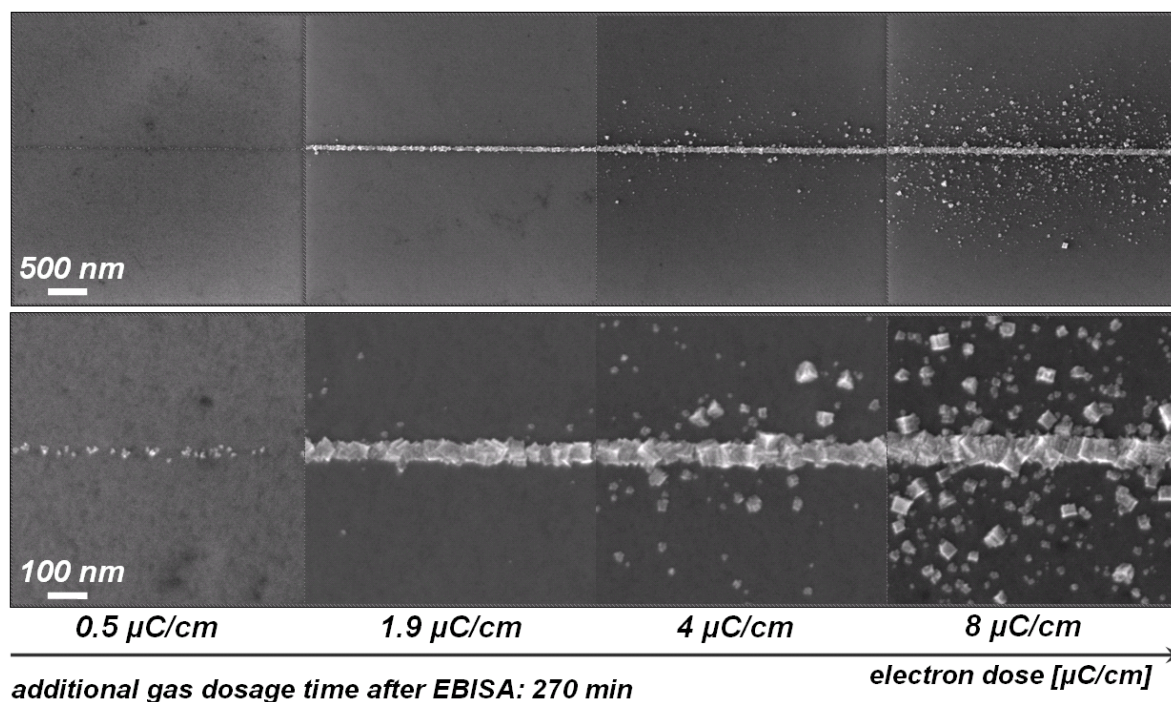


Figure 3.3 Low (upper row) and high (lower row) magnification SEM images of Fe line deposits fabricated by (1) irradiation of the 300 nm SiO<sub>x</sub> on Si(001) with the focused electron beam (0.5 – 8 μC/cm) with no precursor gas in the chamber, and (2) an AGDT of 270 min at  $p(\text{Fe}(\text{CO})_5) = 3.0 \times 10^{-7}$  mbar.

of this thesis, is referred to as electron beam induced surface activation (EBISA). The applied electron doses for EBISA corresponds to the ones of EBID in Figure 3.2. It is obvious that less material is deposited for the EBISA structures via autocatalytic growth, although the AGDT was higher (270 min (EBISA) vs. ~ 250 min (EBID)). This suggests that although for the 1.9 μC/cm EBID deposit at AGDT = 0 min (cf. Figure 3.1) only a darkening of the surface is observed, a significant amount of Fe nuclei is deposited, obviously causing a higher growth rate as compared to EBISA. As for EBISA no deposition occurs during electron irradiation, no FSEs cause unintended deposits in the vicinity of the PE impact point. Thus, by choosing a suitable electron dose and AGDT, the BSE and FSE proximity effect can be suppressed, although a significant amount of material can be deposited via autocatalytic dissociation.

The activity of the surface upon electron irradiation towards the dissociation of Fe(CO)<sub>5</sub> is attributed to O vacancies which are generated by ESD of oxygen (O<sup>+</sup>) via a Knotek – Feibelman mechanism. [44, 69, 70] The active SiO sites cause the initial dissociation of Fe(CO)<sub>5</sub>, which is then followed by autocatalytic growth upon prolonged precursor dosage. The decomposition of Fe(CO)<sub>5</sub> on specially modified sites (e.g. generated by Ga<sup>+</sup> impact) has been reported before, however solely at elevated

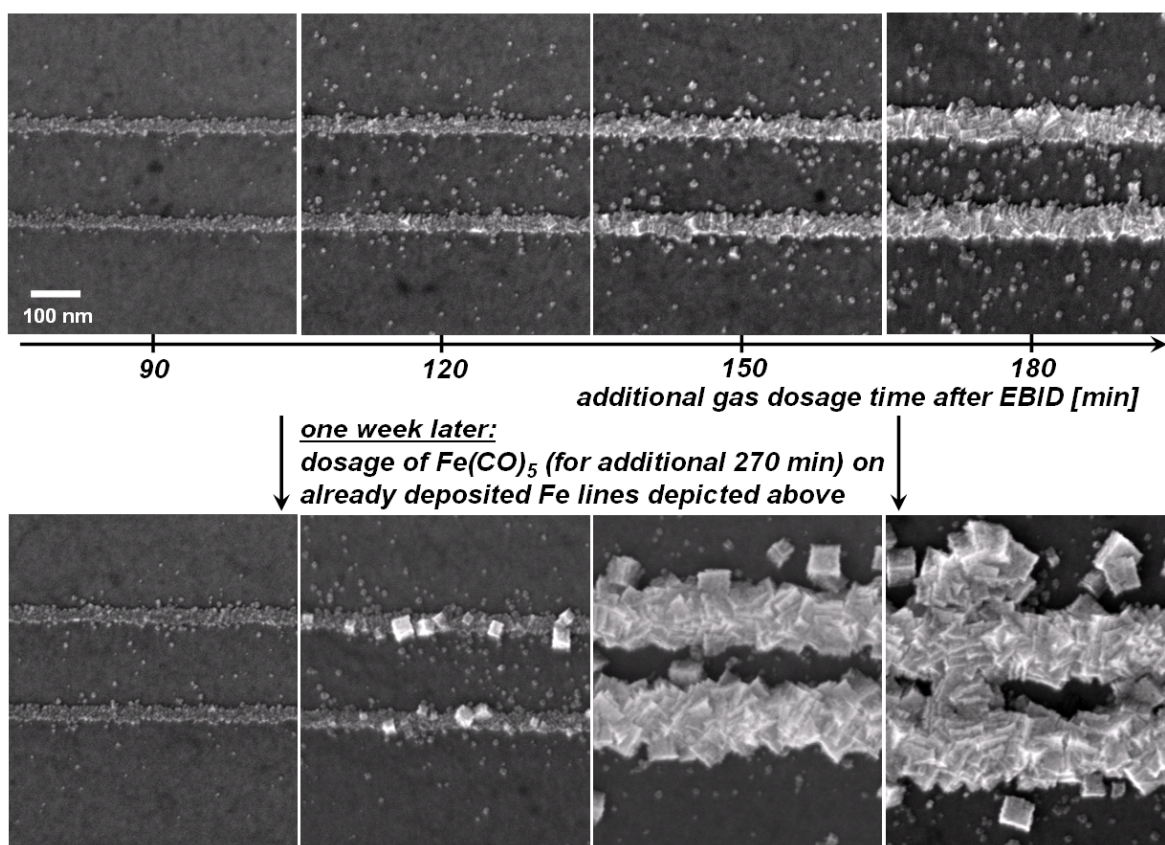


Figure 3.4 SEM images of Fe line deposits fabricated via EBID (each line  $\sim 1 \mu\text{C}/\text{cm}$ ) and varying AGDT (90 – 180 min),  $p(\text{Fe}(\text{CO})_5) = 3.0 \times 10^{-7}$  mbar, before (upper row) and after (lower row) additional exposition to  $\text{Fe}(\text{CO})_5$  for 270 min,  $p(\text{Fe}(\text{CO})_5) = 3.0 \times 10^{-7}$  mbar. Note that the SEM positions are not identical due to influence of imaging.

temperatures. [49] In contrast to this, the Fe structures shown in this thesis are grown at RT. The autocatalytic growth of Fe at RT upon AGDT appears to proceed solely under UHV conditions [71], as for HV conditions, increased sample temperatures, mostly around 450 K, have been reported in literature [47]. The cleanliness of the sample is of high importance for the surface activation and the autocatalytic growth. For samples with a high level of C contamination these processes are either reduced or even strongly inhibited, which might be interpreted as blocking of active and / or adsorption sites. The UHV conditions enable to maintain a clean surface and ensure a preservation of the activated sites for at least two days.

Regarding a possible deactivation by blocking of active sites an interesting phenomenon was observed when dosing  $\text{Fe}(\text{CO})_5$  a second time one week later onto already fabricated EBID Fe line deposits. In Figure 3.4 four EBID double lines ( $\sim 1 \mu\text{C}/\text{cm}$ ) are depicted, which show a transition from a more granular (AGDT = 90 min, cf. Figure 3.4, upper row) to a polycrystalline structure (AGDT = 180 min). Upon second  $\text{Fe}(\text{CO})_5$  dosage, additional autocatalytic growth was only observed on prior polycrystalline

### 3. Results

---

structures (cf. *Figure 3.4*, lower row), i.e. the smaller Fe clusters (AGDT = 90 min,  $d_{\text{mean}} = 6 \text{ nm} \pm 2 \text{ nm}$ ) do not exhibit autocatalytic activity anymore. This observation might be explained by a passivation of the iron due to dissociation of residual gases, like e.g. CO [52-56], which is more pronounced for the smaller clusters than it is for larger crystals. This phenomenon would be in line with the fact that very small nanoparticles, smaller than about 10-20 nm, might exhibit unique chemical properties, which essentially vanish, when they reach 40 or 50 nm. [9] For example, CO adsorbs readily on small Au particles (< 5 nm) on a ZrO support, which is not observed for diameters > 10 nm. Such a size dependent chemical reactivity is explained by change of the surface-to-volume ratio and in particular by a significantly altered electronic structure of small nanoparticles. [72]

### 3.2. On the nature of the activated sites [P2]

The deposition of Fe was studied on an *in situ* prepared ultra-thin SiO<sub>x</sub> film on Si(001), by a combination of catalytic and autocatalytic dissociation of Fe(CO)<sub>5</sub> at RT, with the goal to obtain additional insight into the growth mechanism of the Fe nanocrystals and the nature of the active sites. Particularly, it was of interest to elucidate a possible influence of local charging on the dissociation of Fe(CO)<sub>5</sub> by comparing the ultra-thin to the thick films. Furthermore, the *in situ* fabrication allows for the preparation of very clean SiO<sub>x</sub> films, and thus, to exclude an influence due to a carbon contamination.

In *Figure 3.5a*, an SEM image of such an ultra-thin SiO<sub>x</sub> layer, prepared *in situ* on Si(001) by thermal oxidation, is depicted, which displays a rather rough morphology. By means of local AES an average thickness of ~ 0.5 nm was determined. To investigate the reactivity of this as-prepared film towards the decomposition of Fe(CO)<sub>5</sub>, the surface was exposed to the precursor at RT without pre-activation with electrons. The SEM image acquired after this procedure is shown in *Figure 3.5b*. Interestingly, Fe nanocrystals are observed scattered on the whole surface, indicating that the ultra-thin oxide film initially contains a certain amount of active sites for Fe(CO)<sub>5</sub> dissociation even without electron irradiation. The observation of active sites on the “as is” sample is somewhat unexpected, since commercial 300 nm SiO<sub>x</sub> films on Si(001) were found to be inert towards the decomposition of Fe(CO)<sub>5</sub>. The growth process involving the catalytic decomposition of Fe(CO)<sub>5</sub> at active sites and the successive autocatalytic growth, resulting in Fe nanocrystals, is sketched below the SEM images in *Figure 3.5*. The shape of the Fe crystals is cubic, which is in line with the growth of pure *bcc*  $\alpha$ -iron crystals. [73, 74]

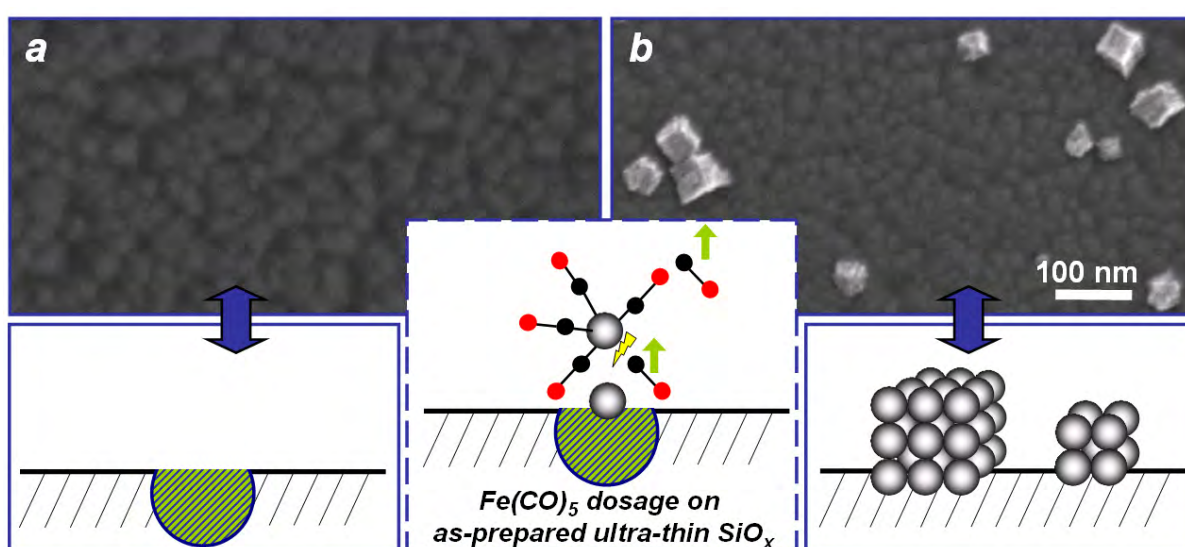


*Figure 3.5* SEM image of as prepared ultra-thin SiO<sub>x</sub> film on Si(001) before (a) and after (b) Fe(CO)<sub>5</sub> dosage (270 min, 3.0 x 10<sup>-7</sup> mbar). Below, schematic drawing of the process.

### 3. Results

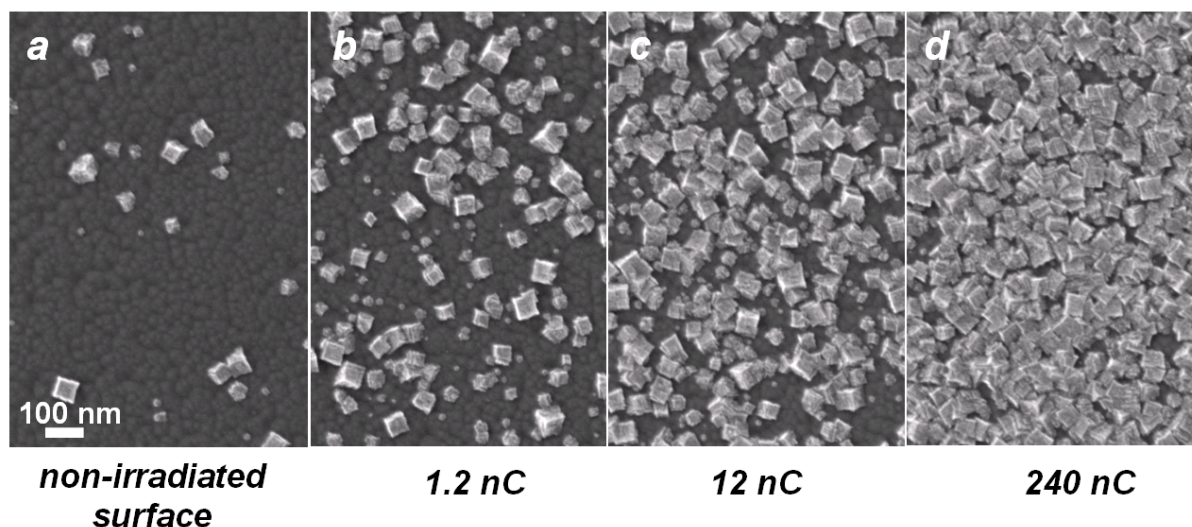


Figure 3.6 SEM images of Fe crystals grown via an AGDT of 270 min at a background pressure of  $3.0 \times 10^{-7}$  mbar on the non-irradiated ultra-thin  $\text{SiO}_x$  on  $\text{Si}(001)$  surface, and on pre-irradiated regions (point irradiation 1.2, 12 and 240 nC, approx. at the center of the SEM images).

Their size is dependent on the AGDT; for the applied parameters crystallites with dimensions up to  $\sim 75$  nm were grown. The purity of the crystals and the absence of Fe and C between them is confirmed by AES. To investigate the influence of electron irradiation, the ultra-thin  $\text{SiO}_x$  film was locally irradiated with a focused electron beam (point irradiation;  $U_{PE} = 15$  kV,  $I_{PE} = 400$  pA,  $\varnothing \sim 3$  nm) with no precursor gas in the chamber. Thereafter, the surface was exposed to  $\text{Fe}(\text{CO})_5$ , following the two-step procedure of EBISA presented in *Chapter 3.1*. The SEM images, obtained after applying this procedure with increasing electron doses and the same AGDT as before, are shown in *Figure 3.6*; clearly, an enhanced deposition of iron is observed in comparison to the non-irradiated surface. It is evident that additional active sites are generated and that these are not restricted to the electron beam impact point (diameter of the electron beam  $\sim 3$  nm), which can be explained by scattering of PEs in the sample, i.e. the BSE proximity effect [26] (cf. *Chapter 3.3*). An analysis of the high magnification SEM images depicted in *Figure 3.6* yields a surface coverage of  $\sim 3\%$  for the non-activated surface, of  $\sim 32\%$  for an electron dose of 1.2 nC,  $\sim 61\%$  for 12 nC and finally  $\sim 90\%$  for 240 nC.

The fact that electron irradiation increases the surface activity also for the ultra-thin layers ( $\sim 0.5$  nm), where no charging is expected due to the close vicinity of the Si substrate, allows us to exclude local charging as the main source for the initial  $\text{Fe}(\text{CO})_5$  decomposition, which could not be completely ruled out for the 300 nm thick  $\text{SiO}_x$  layer. In addition, the activity of the as-prepared ultra-thin  $\text{SiO}_x$  film towards the  $\text{Fe}(\text{CO})_5$  dissociation suggests that structural defects (like e.g. vacancies) are responsible for the

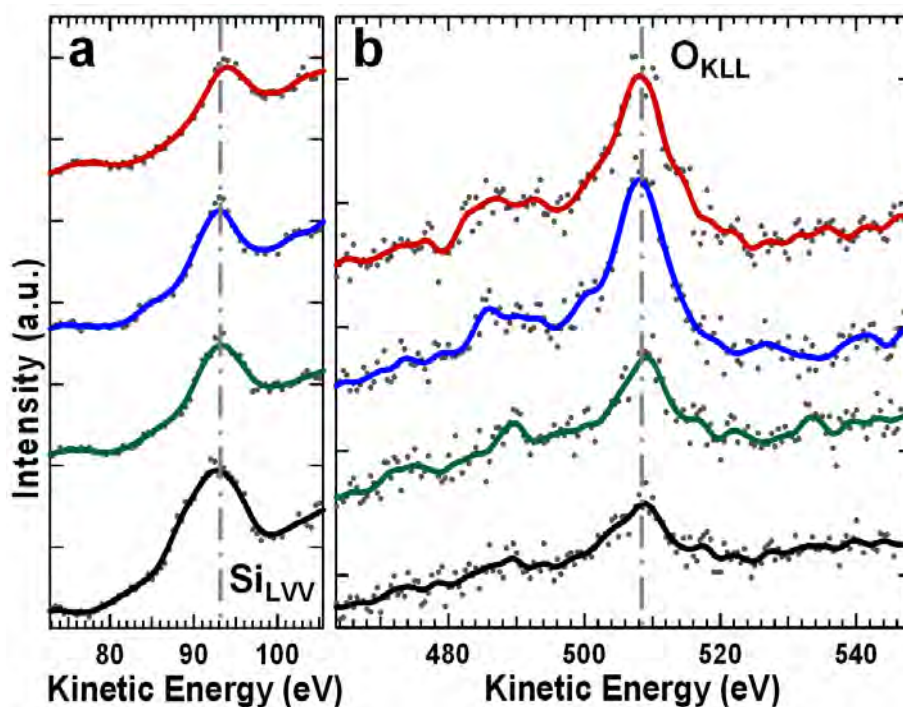


Figure 3.7 Local AES (a) Si LVV and (b) O KLL spectra of the as-prepared ultra-thin  $\text{SiO}_x$  on Si(001) sample after irradiation with increasing local electron area dose  $d_A$ . red: acquisition area  $A = (11\,430 \times 8575) \text{ nm}^2$ ,  $d_A(\text{Si LVV}) = 0.12 \text{ C/cm}^2$ ,  $d_A(\text{O KLL}) = 0.64 \text{ C/cm}^2$ ; blue:  $A = (2287 \times 1715) \text{ nm}^2$ ,  $d_A(\text{Si LVV}) = 3 \text{ C/cm}^2$ ,  $d_A(\text{O KLL}) = 16 \text{ C/cm}^2$ ; green:  $A = (200 \times 200) \text{ nm}^2$ ,  $d_A(\text{Si LVV}) = 300 \text{ C/cm}^2$ ,  $d_A(\text{O KLL}) = 1.6 \times 10^3 \text{ C/cm}^2$ ; black:  $A$ : point scan (diameter 6 nm),  $d_A(\text{Si LVV}) = 4 \times 10^5 \text{ C/cm}^2$ ,  $d_A(\text{O KLL}) = 2 \times 10^6 \text{ C/cm}^2$ .

initial nucleation. X-ray photoelectron spectroscopy investigations of ultra-thin  $\text{SiO}_x$  films by Hollinger and Himpsel, prepared under very similar conditions, provide evidence for the co-existence of sub-oxides in addition to  $\text{SiO}_2$ . [75] The observed reactivity of the as-prepared film therefore indicates that the active sites for the catalytic dissociation are indeed O vacancies or understoichiometric silica.

To gain further insight into the electron induced activation, local AES was performed to determine the amount of oxygen in the ultra-thin  $\text{SiO}_x$  film in dependence on the applied local electron dose. For this purpose AE spectra, shown in Figure 3.7, were acquired by using different scan strategies: the black spectrum was acquired using the spot mode, whereas for the green, blue and red spectrum a certain area (cf. Figure 3.7) was scanned repeatedly, while acquiring the spectrum; thereby the local electron dose is smaller for scanning larger areas, and thus electron induced effects are strongly reduced. The corresponding Si LVV (cf. Figure 3.7a) and O KLL (cf. Figure 3.7b) transitions are observed at  $\sim 93$  and  $\sim 508$  eV, respectively. With increasing local electron dose, a decreasing amount of oxygen is detected, which is accompanied by the concomitant

### 3. Results

---

increase in the Si signal originating from a reduced damping. This observation is in line with the ESD of O via a Knotek–Feibelman mechanism. [44, 70] Analyzing the peak areas of the O *KLL* peaks and assuming an initial composition of SiO<sub>x</sub> of close to x = 2, the formation of SiO<sub>x</sub> with x ≈ 1 at the highest applied electron dose can be estimated. The electron doses applied for local surface activation are comparable to the highest applied electron doses in AES, which suggests that the active species for the Fe(CO)<sub>5</sub> dissociation is SiO.

### **3.3. Investigation of proximity effects for EBISA and EBID [P3, P4]**

One of the challenges in FEBIP are proximity effects. The scattering and the secondary emission of electrons lead to an effective broadening of the processed area compared to the diameter of the primary electron beam. A common strategy to reduce the BSE proximity effect in EBID is to reduce the electron interaction volume by using thin membranes. Therefore, proximity effects were studied by comparing bulk substrates to membranes. It is demonstrated that, contrary to the expectation, proximity effects can be indeed more pronounced on a membrane than on the respective bulk substrate.

In EBID, there is always a superposition of FSE and BSE proximity effects, i.e. these proximity effects cannot be studied separately. However, for EBISA no FSE proximity effect occurs, which is why it can be regarded as a method perfectly suited to study the isolated BSE proximity effect. The investigation of the two bulk samples, SiN-bulk and Si-bulk, and the two membranes, SiN-200nm and SiN-50nm, all covered with a thin native silicon oxide layer (~ 1 nm), expands the EBISA concept from the so far tested thermal (cf. *Chapter 3.1 & 3.2*) to native silicon oxide films. The growth mechanism of the native silicon oxide is considered entirely different from that of the thermal oxide. While Si can be thermally oxidized with pure O<sub>2</sub>, the growth of native oxide (at RT) requires the co-existence of O<sub>2</sub> and H<sub>2</sub>O. [76] Therefore, the structure of the thermal and the native oxide may differ, in particular the hydrogen content. In this context it is interesting to note that hydroxyl rich silicon oxide films are more instable in an electron beam than hydroxyl poor films, [69] which is actually confirmed by the experiments.

As the main findings on the bulk substrates and on the membranes are in agreement, solely the results on SiN-bulk and SiN-200nm are discussed. For more details the reader is referred to [P4].

#### ***Electron beam induced surface activation (EBISA) [P3, P4]***

The BSE proximity effect is basically limited by the BSE exit area, which can be approximated by a Monte Carlo (MC) simulation. Therefore, in general a saturation of the deposit area is expected upon high electron doses, which was e.g. already demonstrated by the results shown in *Figure 3.2*.

This general concept could be confirmed for the SiN-bulk substrate, where a saturation of the EBISA deposit area close to the MC simulated BSE exit area value was observed for high electron doses (see *Figure 3.8b, d, e*). Assuming the BSE proximity effect as a main source, this experimental result reflects the trend expected from literature [26] and from MC simulations.

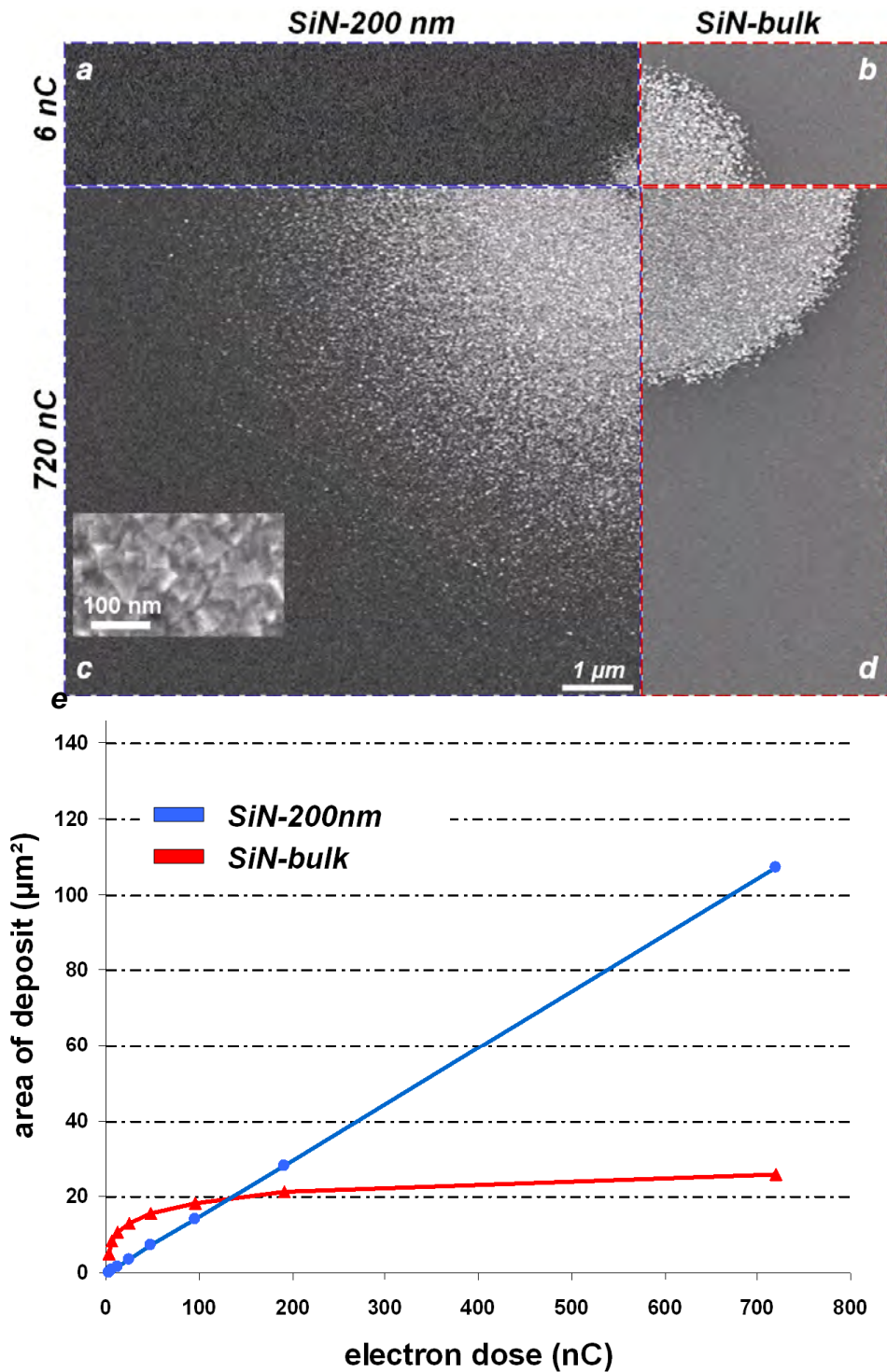


Figure 3.8 SEM images of Fe deposits on SiN-200nm (a & c) and on SiN-bulk (b & d) generated via EBISA applying 6 (a & b) and 720 nC (c & d) (point irradiation,  $I_{PE} = 400$  pA,  $U_{PE} = 15$  kV) and successive autocatalytic growth (AGDT = 270 min,  $p(\text{Fe}(\text{CO})_5) = 3.0 \times 10^{-7}$  mbar). (e) Evaluation of the deposit areas for different applied electron doses on SiN-200nm (blue) and SiN-bulk substrate (red).

The active sites for  $\text{Fe}(\text{CO})_5$  dissociation on SiN-bulk are suggested to be also O vacancies, based on electron dose dependent AES measurements. For the SiN-200nm membrane, where a less pronounced BSE proximity effect is expected compared to the bulk sample, this is only the case for low electron doses (cf. *Figure 3.8a, b*), for the high electron dose a qualitatively different and unexpected behavior is observed: the EBISA deposit on the membrane is now larger than on the bulk substrate (cf. *Figure 3.8c, d*). This contradicts the expectation solely considering electron scattering as source for broadening. While the deposits on SiN-bulk have a rather defined edge, they exhibit a fuzzy boundary on the membrane, consisting of scattered bright spots, which are identified as individual crystallites. When comparing the radius of  $\sim 5.84 \mu\text{m}$  of the high dose deposit on the membrane to the MC simulated value of  $1.5 \mu\text{m}$ , it is evident that this value is too large to be explained by the BSE proximity effect.

To gain further insight, the area of the iron deposits on both substrates was analyzed for different electron doses. While the deposit area on the bulk substrate saturates at a value close to the simulated BSE exit area, as mentioned above, on the membrane interestingly a linear dependence is found (see *Figure 3.8e*). This suggests a correlation of the deposit area with the impinging number of electrons, i.e. charging appears likely to contribute. Generally the bombardment of an insulating thin membrane with high energy electrons yields a positive charging. [77, 78] This was indeed confirmed by corresponding peak shifts in AES measurements (cf. *Figure 3.11*).

The nature of the activity of the pre-irradiated membrane towards  $\text{Fe}(\text{CO})_5$  dissociation is interpreted as being due to chemically modified sites, as observed before. A strong indication for a modification beyond simple charging is that the activity remains for at least one day, with no significant differences of the resulting iron deposits.

The following mechanism for the unexpected broadening of the EBISA deposits on the membrane is proposed: In a first step, electrons are ejected upon high energy electron irradiation, mainly due to SE emission. In a second step, the resulting holes accumulate at the  $\text{SiO}_2 / \text{Si}_3\text{N}_4$  interface, which according to literature is a Si-enriched silicon oxynitride, [79, 80] and which is well known to trap charges. [81-86] Due to the Si enrichment, the interface should be more conductive than the  $\text{SiO}_2$  or the  $\text{Si}_3\text{N}_4$  layer. Therefore, it is likely that a radial transport of the holes along this Si-enriched interface can occur, even to areas beyond BSE emission. The linear increase of the deposit area with the applied electron dose can be explained by a simple diffusion model. Coulomb repulsion of the positively charged holes, which have initially the highest density close to electron beam impact point, is the driving force for their outwards motion (cf. *Figure 3.9*, discussed below). Along the way, electron transfer (ET) from oxygen to  $\text{Si}^+$  occurs, which finally

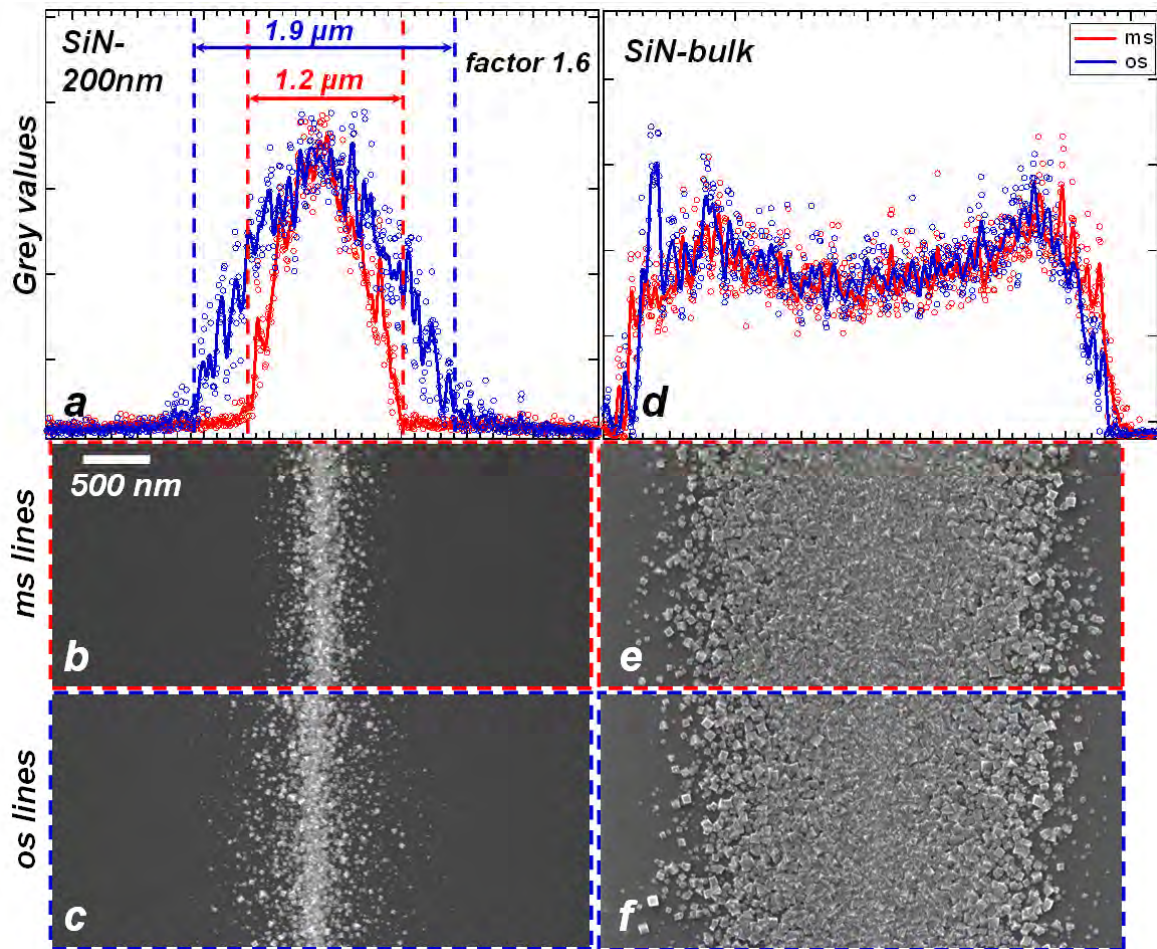


Figure 3.9 Grey value evaluation of EBISA  $16 \mu\text{C}/\text{cm}$  line deposit diameters on SiN-200nm (a) and on SiN-bulk (d) for multiple sweep (ms) lines (red, b and e) and one sweep (os) lines (blue, c and f) (AGDT = 270 min,  $p(\text{Fe}(\text{CO})_5) = 3.0 \times 10^{-7}$  mbar). The indicated diameters correspond to a drop to 10 % of the maximum mean grey value. (Open circles: raw data, solid line: 10 times binomial smooth.)

leads to the formation and desorption of  $\text{O}^+$  species (in analogy to the Knotek-Feibelman mechanism [44, 69, 70]). As soon as one oxygen is consumed per  $\text{SiO}_2$  (i.e.  $\text{SiO}$  is formed [87]), the holes have to travel farther for neutralization. This behavior induces a radial spread of the holes and explains the linear growth of the deposit area with electron dose.

That Coulomb repulsion contributes to the outward motion of the positive charges is indicated by EBISA line deposits on SiN-200nm, depicted in Figure 3.9a-c. The diameter of the EBISA one sweep (os) line (scan velocity,  $v = 0.25 \mu\text{m}/\text{s}$ ) is larger by a factor  $\sim 1.6$  compared to the same electron dose multiple sweep (ms) analog ( $v = 0.15 \text{ m}/\text{s}$ , waiting time after each sweep  $500 \mu\text{s}$ ). Obviously, for the slower scan velocity the holes suffer more effective Coulomb repulsion, leading to a more directed motion of the holes perpendicular to the line than it is the case for the faster beam.

This phenomenon is suggested to be explained by the hole life time. Assuming that every PE causes one hole (i.e. SE coefficient = 1), this means that the hole life time must be larger than time span between two impinging PEs, i.e. 0.4 ns (for  $I_{PE} = 400$  pA), allowing then for Coulomb repulsion. This would explain why the dwell time of the electron beam has an influence on how far the holes travel, i.e. the diameter of the line deposit. It is proposed that when the beam returns for the next sweep (minimum time span 500  $\mu$ s), the holes have then decayed for the most part (e.g. via  $O^+$  desorption), as the multiple sweep line is smaller in diameter than the one sweep line. The same deposits on the SiN-bulk sample show no such behavior, but are very similar in size (see *Figure 3.9d-f*). For this substrate also no charging in the AE spectra was observed.

Other possible mechanisms for surface activation (oxygen desorption), such as electron beam induced heating, backscattering of electrons from underneath the membrane and bending of the membrane have been considered and are excluded to contribute to the observed behavior.

#### ***Electron beam induced deposition (EBID) [P4]***

After understanding the extent of the proximity effects accounting for EBISA on the SiN-bulk sample and on the insulating SiN-200nm membrane, i.e. the BSE proximity effect and the newly introduced “charging” proximity effect, now the more complex EBID process is considered. Here, additionally the FSE proximity effect might play an important role. One of the questions to be clarified is whether on the membrane charging also influences the EBID deposition process.

In *Figure 3.10a-d* SEM images of EBI deposits are depicted, which are directly comparable to the EBISA deposits shown in *Figure 3.8* (same substrates and electron doses). On both substrates, for low electron doses the EBI deposit sizes seem to converge towards the simulated BSE exit area (cf. *Figure 3.10e*), while for higher electron doses it increases beyond. This can be explained by an initially prevailing BSE proximity effect, which is then superimposed by the FSE proximity effect. [88-90] For this latter proximity effect there are clear indications on the bulk substrate. Ray-like deposits appear in the surrounding of the high electron dose deposits, which can be explained by forward scattering of PEs in the central growing tip (see *Figure 3.10d*).

For the membrane, it is obvious that a broadening beyond the BSE exit area starts even at a lower electron dose than on the SiN-bulk substrate, indicating a higher growth rate of the central tip, which is confirmed by the experimental result for the highest applied electron dose (720 nC); here, the diameter is  $\sim 49$   $\mu$ m on SiN-200nm compared to

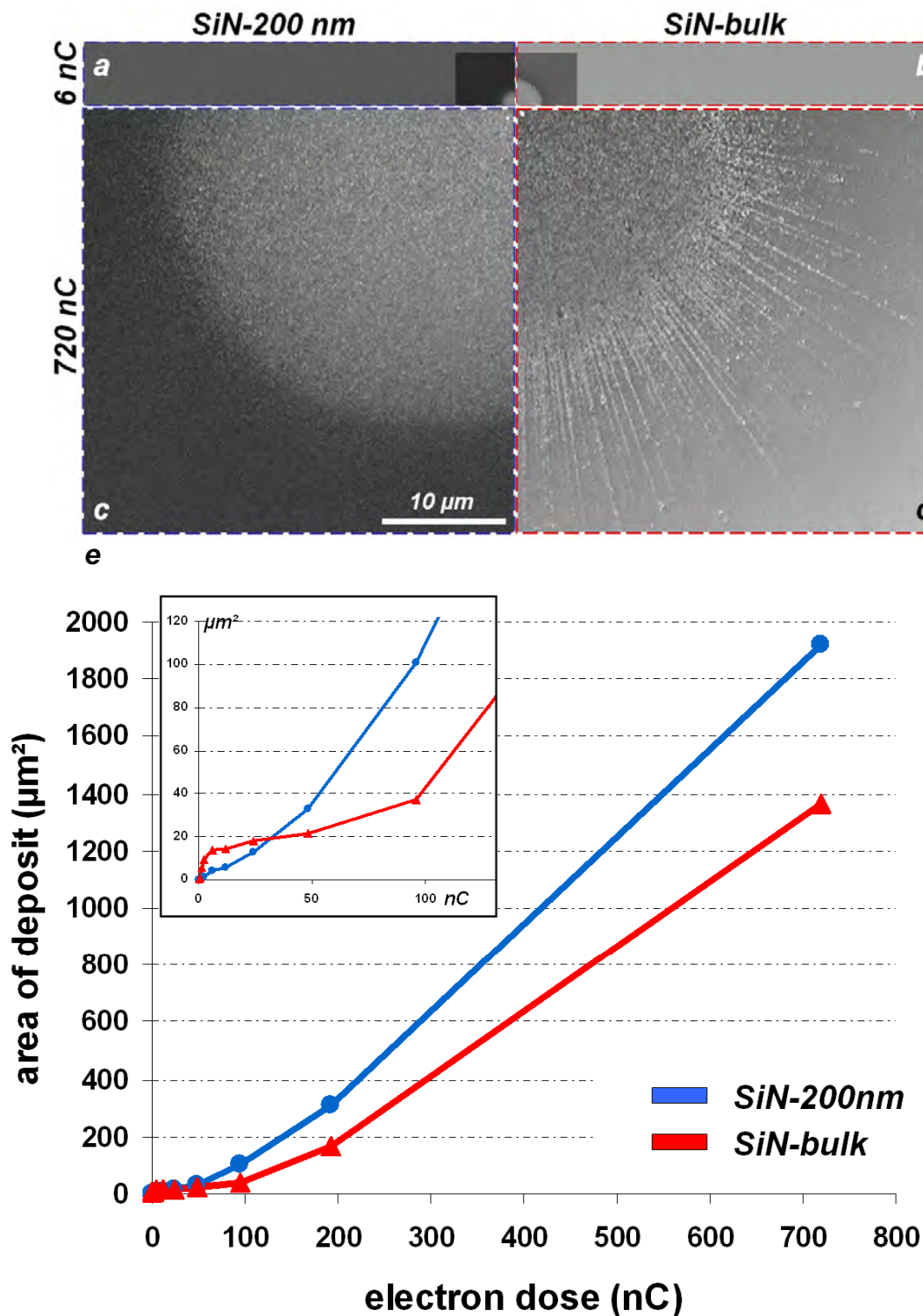


Figure 3.10 SEM images of Fe deposits on SiN-200nm (a & c) and on SiN-bulk (b & d) generated via EBID applying 6 (a & b) and 720 nC (c & d) (point irradiation,  $I_{PE} = 400$  pA,  $U_{PE} = 15$  kV) and successive autocatalytic growth (AGDT is  $\sim 249$  min for 6 nC and  $\sim 197$  min for 720 nC,  $p(\text{Fe}(\text{CO})_5) = 3.0 \times 10^{-7}$  mbar). (e) Evaluation of the deposit areas for different applied electron doses on SiN-200nm (blue) and SiN-bulk substrate (red).

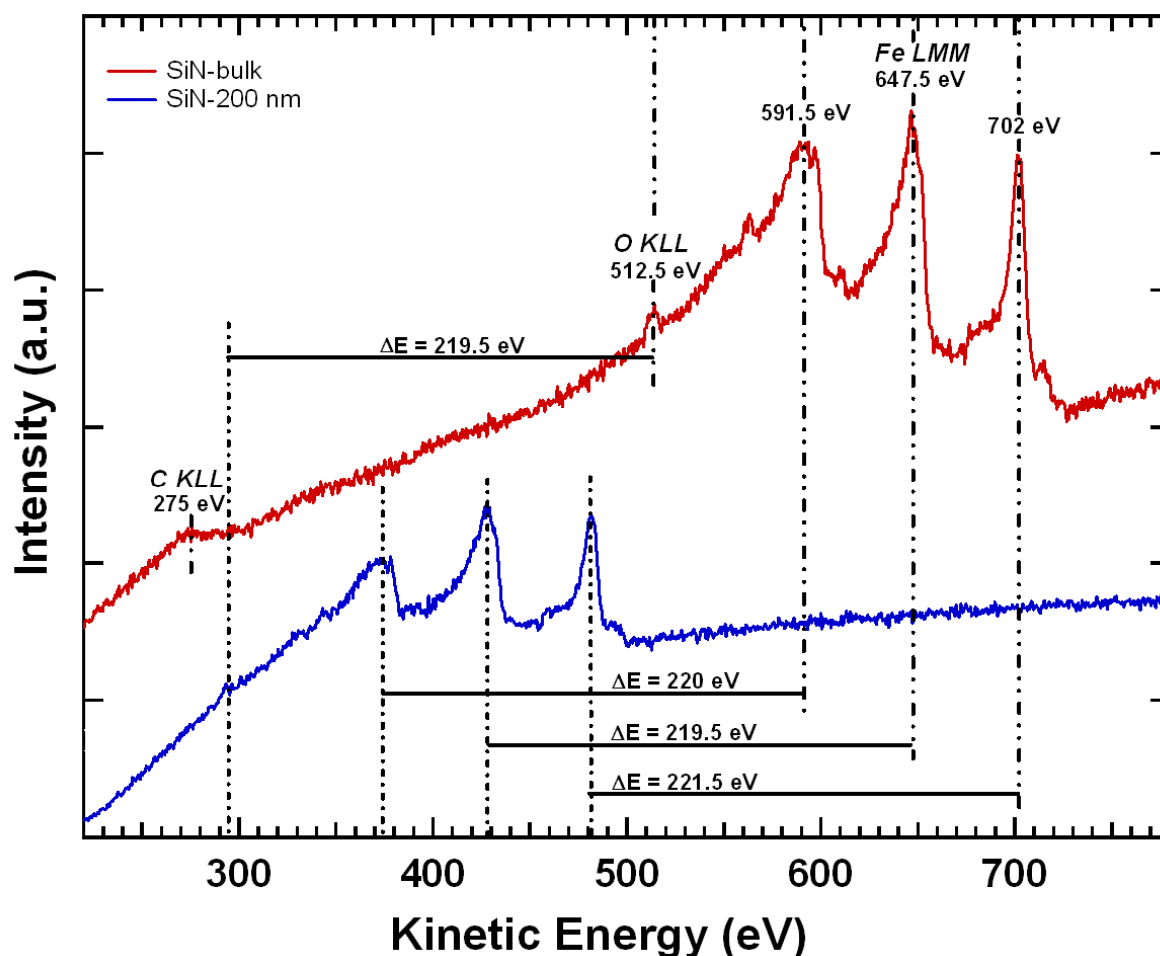


Figure 3.11 AES data acquired ( $I_{PE} = 3 \text{ nA}$ ,  $U_{PE} = 15 \text{ kV}$ ) on an EBISA iron deposit ( $720 \text{ nC}$ ,  $AGDT = 270 \text{ min}$ ,  $p(\text{Fe}(\text{CO})_5) = 3.0 \times 10^{-7} \text{ mbar}$ ) on SiN-bulk (red) and on SiN-200nm membrane (blue).

$\sim 42 \mu\text{m}$  on SiN-bulk. At this point it should be noted, that according to simulation, the BSE coefficient of SiN-200nm is smaller by a factor of 5, giving thus no explanation for a higher growth rate.

To a certain extent the widening on the membrane is interpreted as being due to FSEs, assumed due to the slightly asymmetric shape of the high electron dose deposits. Yet, there are no clear-cut indications for the FSE proximity effect, such as the ray-like structures found on the bulk sample.

Based on these observations (in particular the higher growth rate on the membrane), it is proposed that charging also influences the EBID deposition process, as observed for EBISA. [P3] This is also indicated by Auger data (cf. Figure 3.11) acquired on an iron deposits on SiN-200nm (blue) as compared to SiN-bulk (red). The red spectrum is dominated by Fe LMM transitions ( $\sim 591.5, 647.5, 702 \text{ eV}$ ) and shows small C KLL ( $\sim 275 \text{ eV}$ ) and O KLL signals ( $\sim 512.5 \text{ eV}$ ), confirming the high purity of the autocatalytically

### 3. Results

---

grown Fe deposits. In the blue spectrum, acquired on the iron deposit on the membrane, the *Fe LMM* and *O KLL* transitions are shifted by ~ 220 eV to lower kinetic energy, which indicates a positive charging. Thus, it is proposed that there is also a positive charging during EBI deposition. Oriedo and Russell showed that an electron transfer from an  $\text{Fe}(\text{CO})_5$  molecule to another  $\text{Fe}^+$  ion can cause the dissociation of the molecule, [91] i.e. a dissociative electron transfer from the precursor to the positively charged formed deposit might enhance indeed the deposition rate, as suggested above.

High EBID deposition rates have been reported on SiN-membranes (10 and 50 nm) compared to amorphous C foils when using  $\text{W}(\text{CO})_6$  and 200 kV acceleration voltage; they were attributed to charging effects. [92] Influence on the growth behavior due to charging was also observed on insulating  $\text{Al}_2\text{O}_3$  membranes. [93] Interestingly, even on a semiconducting bulk substrate charging may influence the growth process, when an insulating material is deposited. [94]

### 3.4. Fabrication of Fe deposits for electrical- & magnetotransport measurements [P5]

To characterize the physical properties of the Fe deposits in detail, microwires were fabricated for electrical- and magnetotransport measurements on a 300 nm SiO<sub>x</sub> on Si(001) substrate by a combination of EBID (1.9 μC/cm) and successive autocatalytic growth (AGDT ≈ 270 min) at RT. The specimen was provided by our cooperation partner from the Goethe University Frankfurt (Prof. Dr. Michael Huth), who also performed the conductivity and magnetization measurements.

The specimen is equipped with six gold (Au) contacts (prepared by standard UV photolithography, height 120 nm) to enable contacting the Fe wires for the measurement (cf. Figure 3.12a). As adhesive layer a thin chromium (Cr) film is deposited underneath the Au. Three Fe wires connect the six contacts in a double-cross shaped way.

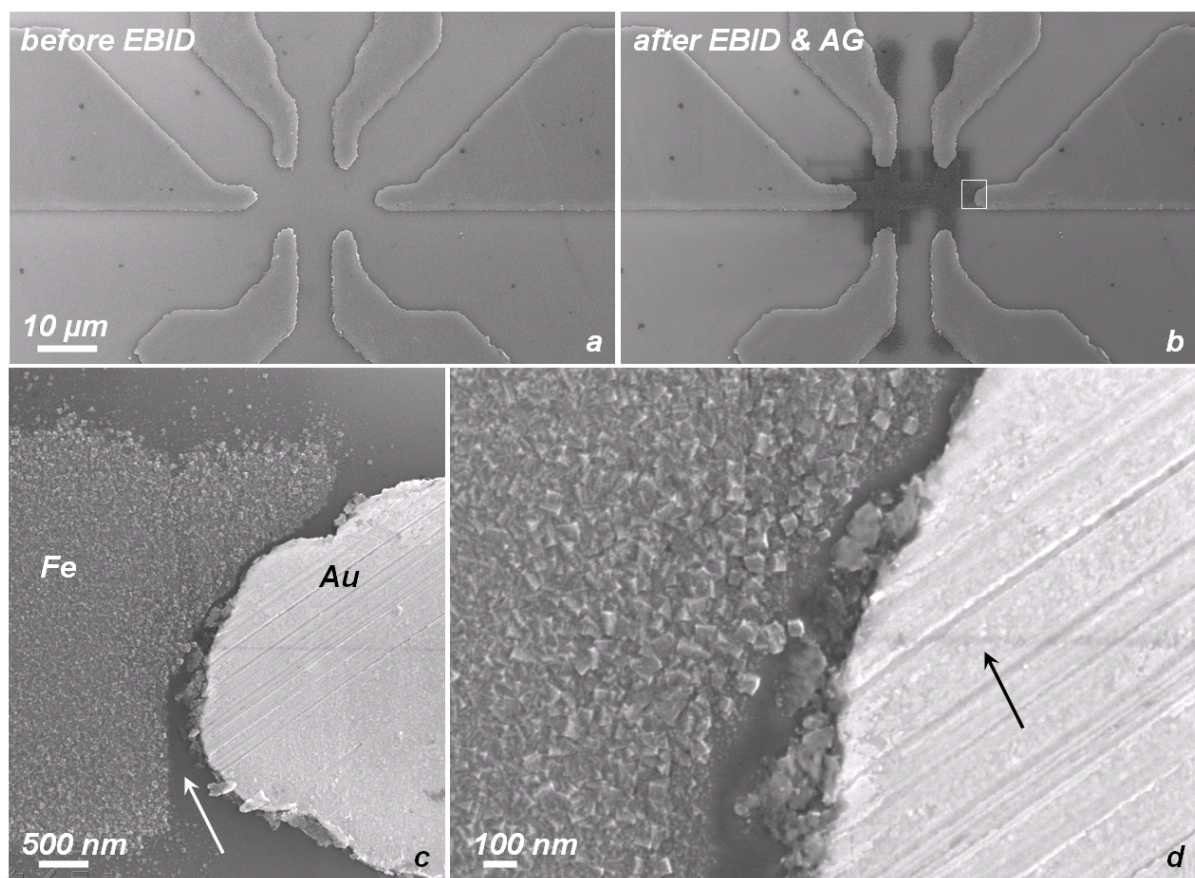


Figure 3.12 SEM image of the sample for electrical- and magnetotransport measurements (a); three Fe microwires (double-cross shaped) bridging the six Au contacts on 300 nm SiO<sub>x</sub> on Si(001) fabricated via EBID (1.9 μC/cm) and an AGDT of 270 min,  $p(\text{Fe}(\text{CO})_5) = 3.0 \times 10^7$  mbar (b); high magnification SEM images highlighting (c) the gap between the iron wire and the Au contact (white arrow) and (d) the line deposit on the Au contact (black arrow).

### 3. Results

---

An overview of this set-up is depicted in *Figure 3.12b*. The width of the iron lines is roughly 4  $\mu\text{m}$ , which is in line with the BSE proximity effect. The wire is composed of Fe crystallites with a typical size of  $\sim 50 \text{ nm} \pm 11 \text{ nm}$ . The length of the Fe microwires was  $\sim 45 \mu\text{m}$ , bridging the gaps between the gold contacts in excess, to ensure a sufficient electrical contact. The original path of the electron beam can be recognized as a narrow, dark line on the Au contacts (cf. *Figure 3.12d*, black arrow). These narrow lines stem from the EBID process itself. Obviously, much less material has been deposited on the Au, proving that the autocatalytic growth is much less efficient than it is on the  $\text{SiO}_x$ . In principle, autocatalytic growth is possible on Au, which is shown later in this chapter. It is speculated that in this case the autocatalytic growth was mostly inhibited due to a possible carbon contamination.

The sensitivity of the autocatalytic growth on the nature of the local substrate is also evident when inspecting the gap between the Au contact and the polycrystalline Fe wire (cf. *Figure 3.12c*, white arrow). This observed effective inhibition of the autocatalytic growth is discussed in detail below. For the measurements this gap was bridged by a low-resistance W-C-Ga-based ion beam induced deposit using the precursor  $\text{W}(\text{CO})_6$ . The transport measurements were performed several days after structure generation, with the samples being stored at ambient conditions in the meantime. Therefore, the surface of the Fe is certainly oxidized, which might be detrimental to the electrical- and magneto-transport properties of the microwires.

The temperature dependent measurement of the Fe microwires showed a typical metallic behavior. The RT resistivity value is about 88  $\mu\Omega \text{ cm}$ , which is about 9 times higher compared to the bulk value ( $\sim 10 \mu\Omega \text{ cm}$ ). This is the lowest value reported so far for Fe deposits fabricated from  $\text{Fe}(\text{CO})_5$ . [7, 95, 96] Furthermore, this resistivity is in the same order of magnitude than measured for cobalt nanowires [97], which is the lowest for EBID deposits from carbonyl precursors in general. This is remarkable since the structures are expected to be partially oxidized, as mentioned above. Besides the resistivity measurements of the microwires, also the magnetotransport properties have been studied. The saturation magnetization of the wires is about 1.47 T which is only about 1.4 times smaller than the bulk value (2.1 T). Measurement of the magnetization in dependence on an external magnetic field shows a hysteresis, proving the ferromagnetic behavior of the Fe microwire. Overall the magnetotransport behavior of the microwires is comparable to Fe thin films reported in literature [98-100]. These measurements confirm the purity of the Fe deposits, which was indicated earlier by AES measurements.

### ***Inhibition of the autocatalytic growth (unpublished results)***

In the following the inhibition of the autocatalytic growth, which was observed phenomenologically as a gap between the Fe wire and the Au contact (cf. *Figure 3.12c*) is further explored. For this purpose, an Fe wire is deposited on a second 300 nm SiO<sub>x</sub> on Si(001) sample, equipped with Au contacts, this time in a parallel arrangement, having again a Cr adhesive layer underneath (successive evaporation of Cr and Au through a stencil mask). The Fe line deposit was fabricated by EBID (1.9 μC/cm) and successive autocatalytic growth (AGDT = 306 min) at RT.

In *Figure 3.13* the SEM image shows the Fe wire bridging the two bright, parallel Au contacts (at the very left and right in the SEM image, cf. labeling). In *region A*, a narrow polycrystalline wire (diameter ~ 100 nm), is observed, which broadens on the SiO<sub>x</sub> (*region B*) to a maximum width of ~ 4 μm, in line with the BSE proximity effect. Adjacent, on the right side of the widened wire, in *region C*, there is almost no Fe deposited. A sharp transition of two different grey values between *region B* and *C* is noted at this position. In *region D*, the narrow polycrystalline wire is observed similar as in *region A*; however, it starts clearly before the bright onset of the Au contact. Also, a broadening at the beginning of the line is observed.

Furthermore, it is noted that there is no sharp transition between the bright Au contacts and the darker substrate (cf. *region A* and *D*). The inset in *Figure 3.13* reveals that small Au islands correspond to this continuous transition.

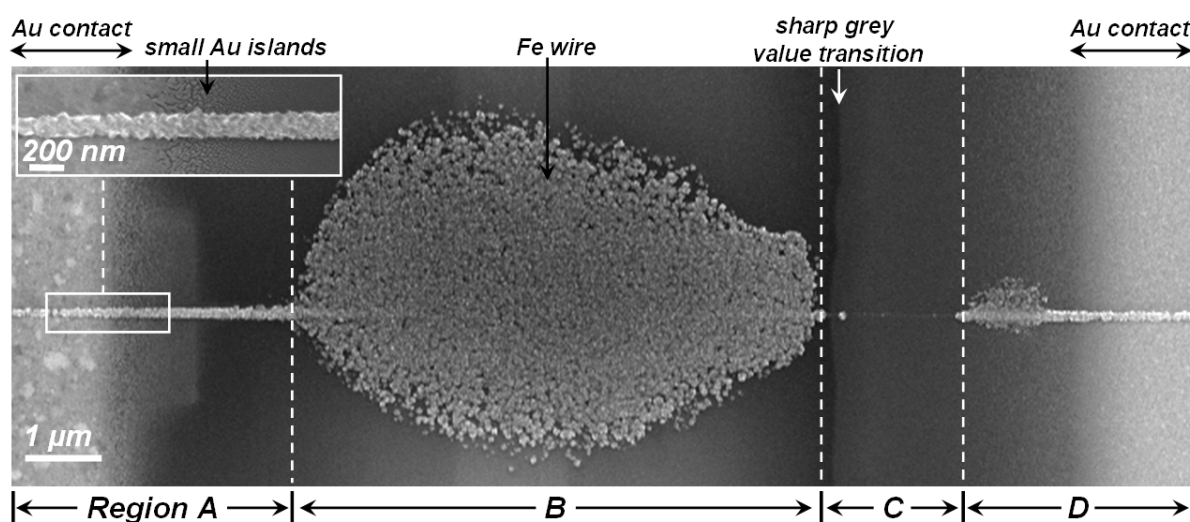


*Figure 3.13* SEM image of an Fe wire on 300 nm SiO<sub>x</sub> on Si(001) bridging two Au contact; the wire was generated via EBID (1.9 μC/cm) and ADGT = 306 min,  $p(\text{Fe}(\text{CO})_5) = 3.0 \times 10^{-7}$  mbar.

### 3. Results

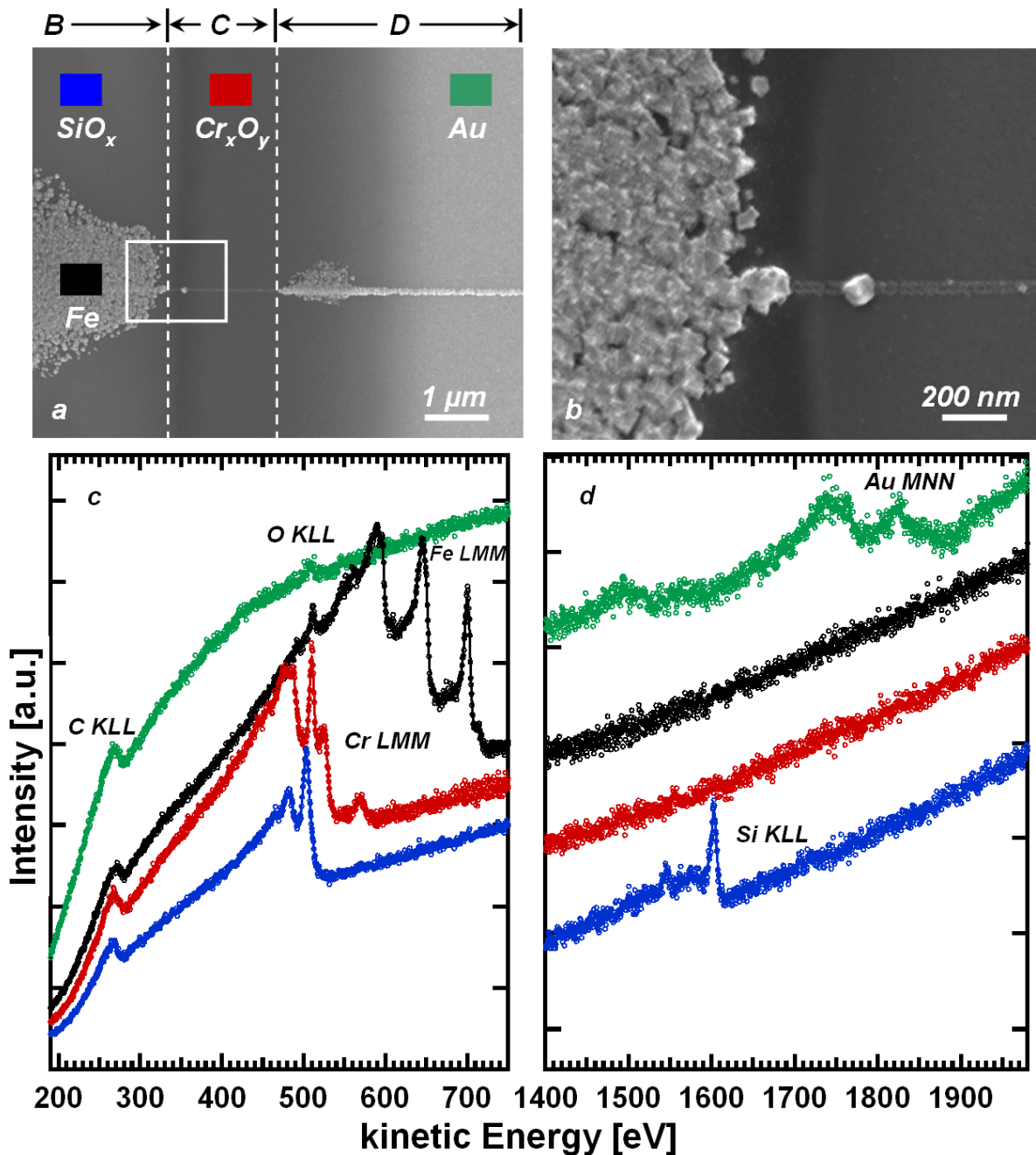


Figure 3.14 (a-b) SEM images of the Fe wire highlighting the position of autocatalytic growth inhibition observed in Figure 3.13, region C. (c-d) AE spectra acquired at similar positions as indicated in (a) (cf. text).

Overall, it can be stated that the deposited amount of Fe significantly differs locally, which is discussed in the following. In Figure 3.14 two SE micrographs are displayed, highlighting the position where almost no Fe is deposited (*region C*). The high magnification SEM image (Figure 3.14b) shows a small line (width  $\sim 45$  nm) of granular morphology, which is mainly attributed to the EBID process itself. The formation of a polycrystalline wire is suppressed, which is explained by a strongly reduced autocatalytic growth. To investigate the source of the inhibition of the autocatalytic growth in more

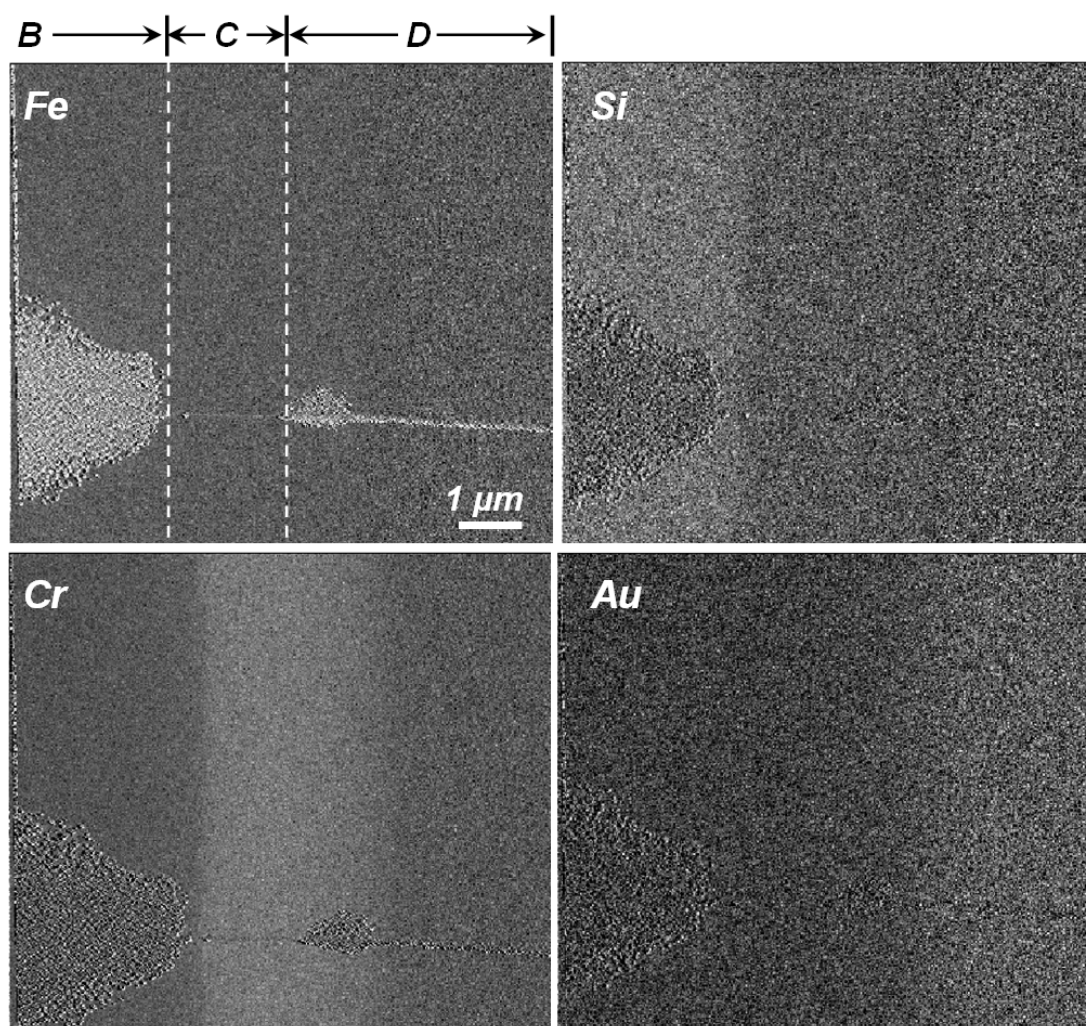


Figure 3.15 SAM images acquired at the SEM position shown in Figure 3.14a for the elements Fe, Si, Cr and Au.

detail, local chemical analysis was performed by means of AES (Figure 3.14c-d). Colored markers in Figure 3.14a indicate the regions, where local AE spectra were collected; the actual AE scans have been acquired at positions different than those indicated to avoid an influence due to imaging. The AE spectra were acquired on polycrystalline Fe (black spectrum), on the  $\text{SiO}_x$  substrate (blue spectrum), in the region where the autocatalytic growth of Fe was inhibited (red spectrum) and on the Au contacts (green spectrum).

In all spectra a minor carbon contamination, i.e. a *C KLL* peak ( $\sim 267$  eV), is observed. The spectrum acquired on the gold contact (green) is dominated by the *Au MNN* transitions ( $\sim 1493, 1737, 1821$  eV); besides, a small oxygen trace is detected (*O KLL* peak,  $\sim 508$  eV). The high purity of the crystalline iron deposit (black spectrum, dominating *Fe LMM* transitions,  $\sim 590, 596, 645, 700$  eV, minor *O KLL* peak,  $\sim 511$  eV) and the chemical composition of the  $\text{SiO}_x$  (blue spectrum, main peaks *Si KLL*,  $\sim 1603$  eV and *O KLL*,  $\sim 503$  eV) is confirmed. The spectrum which is acquired in the region where

### 3. Results

---

the autocatalytic growth of Fe is inhibited (red), displays *Cr LMM* transitions (~ 476, 488, 525, 569 eV) and also a significant *O KLL* peak (~ 510 eV). It is clear that the oxygen signal originates from the Cr layer, since there is no *Si KLL* signal from the underlying  $\text{SiO}_x$  film. Therefore, the adhesive layer was calculated to have at least a thickness of ~ 5 nm (i.e. *Si KLL* damping  $\leq 5\%$  [101]). Another hint that the oxygen peak can be attributed to the Cr layer is that the energy position of the *O KLL* signal is shifted by ~ 7 eV to higher kinetic energy compared to the one of the  $\text{SiO}_x$  layer. Thus, it is concluded that the adhesive layer is actually a thin chromium oxide,  $\text{Cr}_x\text{O}_y$ , film; this is true at least for the part which is not covered by Au.

To check the chemical analysis which was performed off the Fe wire position, scanning Auger electron microscopy (SAM) images were acquired, for the elements Fe, Si, Cr and Au, in the same area as shown in *Figure 3.14a*. In *region C*, where the autocatalytic growth of Fe seems to be inhibited, the Fe signal is significantly reduced, the Si signal is completely suppressed, which is expected from the AES measurement, and instead, a Cr species is detected. The Au contact is observed as faint stripe at the very right of the Au SAM image; the low contrast is due to the small peak height of the *Au MNN* transition in comparison to e.g. the *Si KLL* signal. The SAM data clearly confirms the local AES measurements, i.e. the region where the autocatalytic growth is inhibited is the adhesive chromium layer, which is obviously not completely covered by the Au.

The inhibition of the autocatalytic growth might be explained by (1) changed interaction of the precursor with  $\text{Cr}_x\text{O}_y$  surface compared to e.g.  $\text{SiO}_x$ , (2) the chemical nature of the Fe wire on the  $\text{Cr}_x\text{O}_y$  surface and (3) interaction of the Fe wire with the  $\text{Cr}_x\text{O}_y$ .

(1) An altered adsorption / desorption / diffusion behavior (e.g. reduced residence time, sticking coefficient) of the precursor molecule on the  $\text{Cr}_x\text{O}_y$  surface might lead to a strongly reduced autocatalytic growth and deposition rate in EBID.

(2) Furthermore, the formation of an iron oxide species (O e.g. from  $\text{Cr}_x\text{O}_y$ ), of an iron-chromium-alloy (e.g. electron induced), or of an iron-chromium-oxide species might change the catalytic activity of the iron wire towards  $\text{Fe}(\text{CO})_5$  decomposition.

(3) Also, a lower catalytic activity of the Fe might be explained by an interaction with the  $\text{Cr}_x\text{O}_y$  support or by environment-induced contamination.

All these possible explanations, solely or in combination, could account for the inhibition of the autocatalytic growth. The possibility to tune the growth of Fe by surface modifications, e.g. by a chromium coating, might be exploited as another “tool in the box” for the fabrication of nanostructures. These results show clearly that the surface can play a determining role in the deposition process and thus has to be generally considered.

### 3.5. Fe nanostructures as catalyst for Si nanowire growth (unpublished results)

To investigate the chemical properties of the Fe nanostructures, they were tested as a catalyst for the growth of Si nanowires (NWs) via high temperature chemical vapor deposition (CVD). These experiments were performed by our cooperation partner from the Technical University Vienna (Ass.-Prof. Dr. Alois Lugstein).

The SEM image in *Figure 3.16a* shows Fe nanostructures deposited over several micrometers via EBISA and an AGDT of 270 min on 300 nm SiO<sub>x</sub> on Si(001). The structures exhibit a crystalline morphology, which is in agreement with the results presented so far and in line with the growth of *bcc*  $\alpha$ -iron. The sample was stored at ambient conditions for approximately one week before it was utilized as a catalyst for the Si NW growth. Thus, it is assumed that the surface of the catalyst was oxidized when the experiment was started. However, the Si NWs were grown under reducing conditions, which might lead to the formation of Fe(0) again. This is e.g. well known for the Haber-Bosch process. [102] For the Si NW growth, the precursor molecule octachlorotrisilane (OCTS), Si<sub>3</sub>Cl<sub>8</sub>, is supplied in a He/H<sub>2</sub> gas mixture (100:10 sccm) at a sample temperature of ~ 1170 K. In *Figure 3.16b* an SEM image of the grown Si NWs is depicted.

From *Figure 3.17a* it is obvious that the wires exhibit a variety in length, orientation and crystallinity. In *Figure 3.17b* a high magnification SEM image shows two Si NWs, one of high (the left one) and one of poor (the right one) crystallinity, i.e. high kinking. The diameters of the NWs are in the order of 50 nm. This experiment is a first proof of principle that the EBISA Fe nanostructures can be employed as catalyst and that this allows for the local growth of Si NWs.

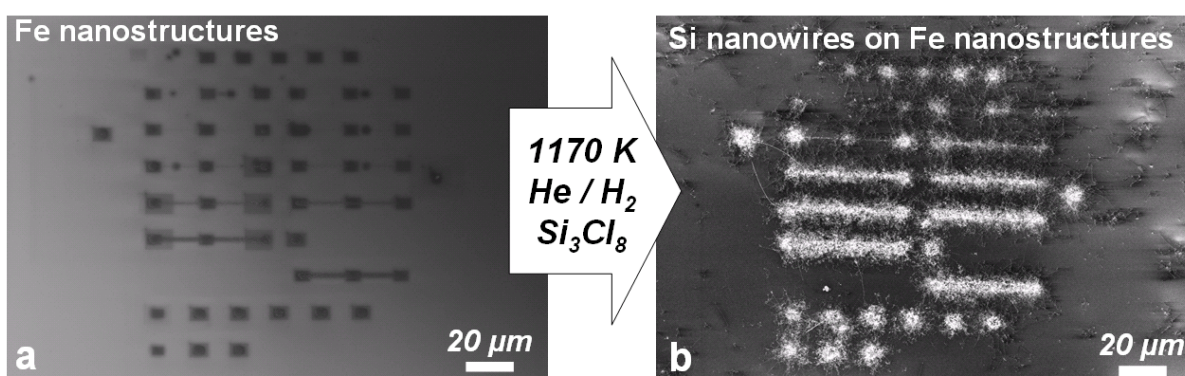


*Figure 3.16* SEM images before (a) and after (b) Si nanowire growth on EBISA Fe nanostructures.

### 3. Results

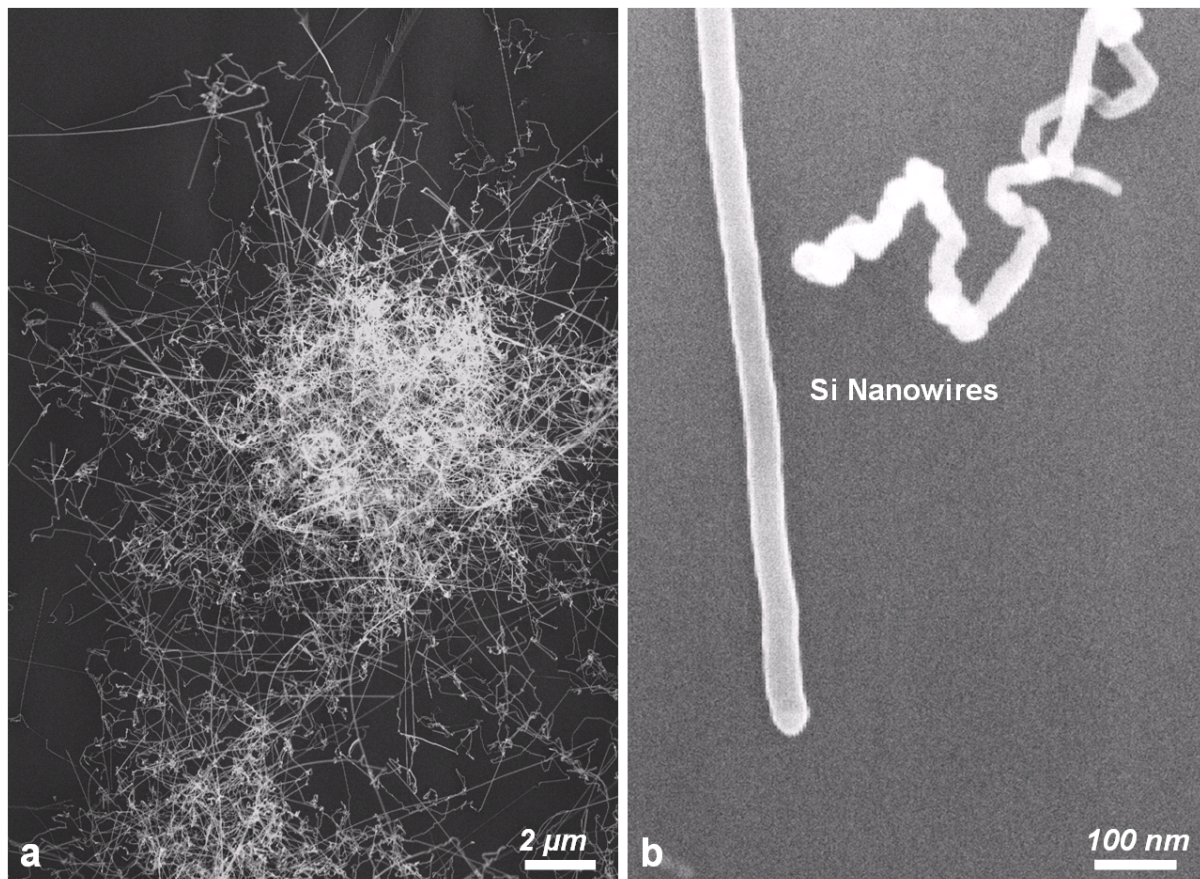


*Figure 3.17 SEM image of locally generated Si nanowires on EBISA Fe nanostructure (a); and high magnification SEM image of two Si nanowires of different crystallinity (b).*

Individual Si NWs were fabricated recently by a combination of focused ion beam milling, EBID and CVD over a Au catalyst [103], which is one of the most frequently applied catalyst material for the Si NW growth [104]. The advantages of Au as catalyst are a ready availability, a high chemical stability and its non-toxicity. The main reason for its frequent use is, however, the low eutectic temperature of the Au-Si binary phase (636 K). The growth of the Si NWs at these liquid Au-Si droplets proceeds via the so-called vapor-liquid-solid (VLS) growth mechanism. The gaseous precursor (vapor) decomposes at the catalyst surface, thereby additional Si is supplied to the catalyst droplet (liquid). At equilibrium only a limited amount of Si can be dissolved in the Au-Si droplet, which then leads to crystallization of the excess Si and the growth of Si NWs (solid). The disadvantage of Au is a significant contamination of the NWs with the catalyst itself, which is associated with strongly enhanced carrier recombination. The high chemical stability of the Au makes it difficult to clean the contaminated Si NWs. [104]

Therefore, a large variety of other catalysts has been tested for Si NW growth. Among these, one successfully applied candidate is Fe [105-110], which is also proven by our experimental result. Besides the VLS mechanism, also the so-called vapor-solid-solid

(VSS) mechanism has been reported for Fe, i.e. the catalyst is solid during the Si NW growth. This growth mode is enabled by silicide formation, i.e. the wires grow via Fe silicide particles. At 1170 K, applied in the above described Si NW growth experiment, the temperature is well below the eutectic temperature of the Fe-Si binary phase (~ 1470 K e.g. [105]), which suggests that the wires shown in *Figure 3.17* are grown in the VSS mode. Si NWs grown in this mode (via silicide particles) show a higher density of crystallographic defects [106] compared to VLS-grown ones [110], which is indeed observed (e.g. see *Figure 3.17b*, right NW). Therefore, it is suggested that this first explorative work, proving that the fabricated EBISA Fe nanostructures can be employed for local Si NW growth, should be expanded to a higher temperature regime (> 1470 K) allowing then for the VLS growth mode and thus for a higher crystalline quality of the wires.



## 4. Summary

In this thesis, clean iron nanostructures were fabricated on various thermal and native silicon oxides via focused electron beam induced processing (FEBIP) techniques followed by successive autocatalytic growth. The applied precursor molecule was iron pentacarbonyl,  $\text{Fe}(\text{CO})_5$ , and the deposition process was performed at room temperature in ultra-high vacuum (UHV). The morphology and the chemical composition of the FEBIP nanostructures was characterized by means of scanning electron microscopy (SEM) and local Auger electron spectroscopy (AES), respectively. The results are presented in a cumulative form; the full papers are attached in the *Appendix*.

Focused electron beams have proven to be a suitable and clean tool to modify chemical properties very locally, which can be exploited for the fabrication of nanostructures on surfaces. A prominent example is electron beam induced deposition (EBID) in which a focused electron beam, e.g. from an electron microscope, is used to induce the dissociation of adsorbed precursor molecules, with the resulting non-volatile fragments forming a deposit. Starting from this technique followed by autocatalytic growth on a thermal 300 nm  $\text{SiO}_x$  on Si(001) substrate, a novel lithographic technique was developed in this thesis: electron beam induced surface activation (EBISA). This two-step procedure significantly expands the EBID concept and relies on the local dissociation of  $\text{Fe}(\text{CO})_5$  at electron pre-irradiated regions. In the course of this process, the chemical properties of the surface are very locally modified (activated) with the electron beam such that it plays an active part in the deposition process. The applied surface science approach has proven to be mandatory to ensure clean surfaces and well defined conditions.

Due to the autocatalytic growth behavior of the precursor  $\text{Fe}(\text{CO})_5$ , the size of the nanostructures can be controlled via the additional gas dosage time after EBID or the EBISA process. Individual iron structures with dimensions between 6 and 75 nm were fabricated. The observed polycrystalline cubic substructure of the iron deposits at high additional gas dosage times is in line with the growth of *bcc*  $\alpha$ -Fe; local AES on the fabricated iron nanostructures revealed a metal content higher than 95 % with the contaminants being carbon and oxygen.

To gain more insight into the mechanism of the EBISA process, investigations on *in situ* prepared ultra-thin  $\text{SiO}_x$  (0.5 nm) on Si(001) were performed. Here, charging of silicon oxide can be excluded due to the close vicinity of the silicon substrate. It was proven by electron dose dependent AES measurements that understoichiometric silica, i.e. oxygen vacancies, are the active sites for  $\text{Fe}(\text{CO})_5$  dissociation. The vacancies are generated via electron stimulated desorption (ESD) of oxygen, presumably via the Knotek-Feibelman

## 4. Summary

---

mechanism. Furthermore, an activity of the *as-prepared* ultra-thin SiO<sub>x</sub> film (without any electron pre-irradiation) towards Fe(CO)<sub>5</sub> dissociation was observed, supporting that indeed structural defects are the active sites.

In addition to the investigations on thermal silicon oxides, the concept of EBISA was also transferred to native silicon oxide on silicon (Si-bulk) and on silicon nitrides (SiN-bulk). On the latter substrate, AES measurements indicated that again oxygen vacancies in the electron pre-irradiated areas might act as active sites for Fe(CO)<sub>5</sub> dissociation. The Si-bulk and the SiN-bulk substrates were compared to silicon nitride membranes (50 and 200 nm) and so-called proximity effects were studied for EBISA and EBID. Proximity effects are unintended deposits in close vicinity to the initial impact point of the focused electron beam caused by scattered electrons and thereby induced secondary electrons.

The technique EBISA is well suited to monitor the size of the backscattered electron (BSE) exit area of a focused electron beam interacting with a (planar) solid material. For EBISA, the superposition of BSEs and forward scattered electrons (FSEs), which occurs during EBID can be ruled out, since no deposits form during electron irradiation.

By using membranes, scattering effects can effectively be reduced by a cutoff of the electron interaction volume. Contrary to the expectation, it was found that proximity effects can in fact be larger on silicon nitride membranes than on the respective bulk substrate. This phenomenon was explained for EBISA by a positive charging effect of the silicon nitride membrane and thereby induced oxygen desorption beyond the BSE exit area. Furthermore, it was demonstrated for the silicon nitride membrane that positive charging of the formed deposit leads to an enhanced EBI deposition rate, as compared to the respective bulk substrates. Other possible mechanisms leading to the observed phenomena, like e.g. electron beam induced heating, have been considered and are excluded. Consequently, when working on silicon nitride membranes in combination with an electron beam, charging effects must be considered.

In the framework of cooperations with the Goethe University Frankfurt (Prof. Dr. Michael Huth) and the Technical University Vienna (Ass.-Prof. Dr. Alois Lugstein) the properties of the generated iron structures were studied further.

Electrical- and magnetotransport measurements showed that the iron deposits exhibit metallic conductivity and ferromagnetic magnetization properties, as expected from clean iron thin films. These measurements support the high purity of the iron nanostructures, which was earlier indicated by AE spectra. During these studies, the phenomenon of the inhibition of autocatalytic growth by chromium oxide was observed, which is another “tool in the box” to tune the morphology of nanostructures. Furthermore, these results prove again the high impact of the substrate on the deposition process.

Finally, it was shown as a first proof of principle that Fe nanostructures produced by EBISA and subsequent autocatalytic growth can be used as a catalyst for the local growth of silicon nanowires via high temperature chemical vapor deposition with the precursor octachlorotrisilane,  $\text{Si}_3\text{Cl}_8$ . At the applied conditions the silicon nanowires were grown in the so-called vapor-solid-solid growth mode via iron silicide particles.

Overall, the results of this thesis demonstrate that the chemical nature of the surface can play a determining role in the deposition process, and thus has to be generally considered.



## 5. Outlook

For future work, it would be interesting to transfer the concept of the novel FEBIP technique EBISA to substrate materials other than silicon oxide, such as vanadium(V)-oxide,  $V_2O_5$ , tungsten(VI)-oxide,  $WO_3$ , or titanium(IV)-oxide,  $TiO_2$ . These materials are well known to be sensitive towards electron irradiation, i.e. electron stimulated desorption of oxygen occurs [44], resulting in possibly active sites for  $Fe(CO)_5$  dissociation. In fact, first explorative work proves that EBISA and successive autocatalytic growth works also on titanium oxide with the precursor  $Fe(CO)_5$ .

Other molecules than  $Fe(CO)_5$  might also dissociate at electron pre-irradiated areas and then grow autocatalytically, with especially promising candidates being the metal carbonyls nickel tetracarbonyl,  $Ni(CO)_4$ , chromium hexacarbonyl,  $Cr(CO)_6$ , and dicobalt octacarbonyl,  $Co_2(CO)_8$ . In particular the latter molecule is an interesting precursor for magnetic applications, as is  $Fe(CO)_5$ .

While iron is basically a ferromagnetic material, it becomes superparamagnetic on the nanoscale, which sets an upper physical limit to data storage density of hard disk drives, known as the superparamagnetic limit. This can be pushed further by using ferromagnetic nanostructures with the highest possible magnetic anisotropy to increase the magnetic stability (concerning thermal fluctuations and magnetic fields), and thus to enable an increase of the data storage density. [111] For this purpose, the FEBIP techniques are an excellent tool to allow for testing different geometrical arrangements and arbitrarily shaped nanostructures, which might increase the magnetic stability.



## 6. Zusammenfassung

Das Ziel dieser Arbeit war die Herstellung reiner Eisen-Nanostrukturen, ausgehend von dem Precursormolekül Eisenpentacarbonyl,  $\text{Fe}(\text{CO})_5$ , auf isolierenden Siliziumoxid-Substraten mittels „Fokussierter Elektronenstrahl-induzierter Prozessierung“ (engl. focused electron beam induced processing, FEBIP) und nachfolgendem autokatalytischem Wachstum im Ultrahochvakuum (UHV). Die Morphologie und die chemische Zusammensetzung der FEBIP-Nanostrukturen wurden mit Hilfe der Rasterelektronenmikroskopie (REM) und der lokalen Augerelektronenspektroskopie (AES) untersucht. Die Ergebnisse sind in einer kumulativen Form dargestellt; die Veröffentlichungen befinden sich im Anhang.

Ein fokussierter Elektronenstrahl ist ein hervorragendes und sauberes Werkzeug um sehr lokal chemische Eigenschaften von Materie zu modifizieren, was für die Herstellung von Nanostrukturen auf Oberflächen genutzt werden kann. In diesem Zusammenhang ist die „Elektronenstrahl-induzierte Abscheidung“ (engl. electron beam induced deposition, EBID) ein bedeutendes Anwendungsbeispiel; hier werden adsorbierte Precursoren unter dem Einfluss eines fokussierten Elektronenstrahls, z.B. von einem REM, dissoziiert und eine Abscheidung bildet sich aus den nicht-flüchtigen Bestandteilen des Precursors. Ausgehend von dieser Technik und nachfolgendem autokatalytischem Wachstum auf thermischem 300 nm  $\text{SiO}_x$  auf  $\text{Si}(001)$ , wurde eine neue lithographische Technik, die „Elektronenstrahl-induzierte Oberflächenaktivierung“ (engl. electron beam induced surface activation, EBISA), entwickelt, welche das EBID-Konzept signifikant erweitert. EBISA basiert auf der lokalen Dissoziation von  $\text{Fe}(\text{CO})_5$  an zuvor mit Elektronen bestrahlten und auf diese Weise aktivierten Flächen. Bei dieser Technik werden die chemischen Eigenschaften der Oberfläche mit Hilfe des Elektronenstrahls lokal so modifiziert, dass sie selbst einen aktiven Part in dem Abscheideprozess einnimmt. Der in dieser Arbeit verfolgte „Surface Science“ Ansatz ist in diesem Zusammenhang besonders wichtig; nur so können saubere Oberflächen und wohldefinierte Bedingungen gewährleistet werden.

Durch autokatalytische Dissoziation von  $\text{Fe}(\text{CO})_5$  an bereits abgeschiedenem Eisen kann die Größe der Nanostrukturen über die zusätzliche Gasdosierungszeit nach dem EBID- oder dem EBISA-Prozess beeinflusst werden. Separate Eisen-Nanostrukturen mit Durchmessern von  $\sim 6 - 75$  nm wurden hergestellt. Die polykristalline kubische Substruktur der Eisenabscheidungen, die bei hohen zusätzlichen Gasdosierungszeiten beobachtet wird, ist ein Hinweis auf das Wachstum von *bcc*  $\alpha$ -Eisen. Lokale AES-Messungen belegen die hohe Reinheit von 95 % Eisen, mit Kohlenstoff und Sauerstoff als Kontaminationen.

## 6. Zusammenfassung

---

Das mechanistische Verständnis des EBISA-Prozesses wurde auf *in situ* präpariertem, thermischem ultra-dünne SiO<sub>x</sub> (0.5 nm) auf Si(001) vertieft. Hier kann eine Aufladung des Siliziumoxids aufgrund der geringen Schichtdicke ausgeschlossen werden. Mittels elektronendosisabhängiger AES-Messungen wurde gezeigt, dass die aktiven Zentren für die Zersetzung von Fe(CO)<sub>5</sub> unterstoichiometrisches Siliziumdioxid sind. Die Sauerstoff-Fehlstellen werden durch elektronenstimulierte Desorption generiert, wahrscheinlich über den Knotek-Feibelman-Mechanismus. Des Weiteren wurde beobachtet, dass der ultra-dünne SiO<sub>x</sub>-Film schon ohne vorangegangene Elektronenbestrahlung eine Aktivität bezüglich der Fe(CO)<sub>5</sub>-Dissoziation aufweist, welches die Annahme, dass tatsächlich strukturelle Defekte die aktiven Zentren sind, unterstützt.

Nach den Untersuchungen auf thermischen Siliziumoxiden konnte das EBISA-Konzept auch auf natives Siliziumoxid auf Silizium (Si-bulk) und Siliziumnitrid (SiN-bulk) übertragen werden. Bei letzterem Substrat legen AES-Messungen nahe, dass hier ebenfalls Sauerstoff-Fehlstellen in den mit Elektronen bestrahlten Flächen als aktive Zentren für die Dissoziation von Fe(CO)<sub>5</sub> dienen. Die beiden Proben, Si-bulk und SiN-bulk, wurden mit Siliziumnitrid-Membranen (50 und 200 nm) verglichen und sogenannte „Proximity-Effekte“ wurden für EBISA und EBID untersucht. Proximity-Effekte sind unbeabsichtigte Abscheidungen in der Nähe des Auftreffpunktes des fokussierten Elektronenstrahls aufgrund gestreuter Elektronen und dadurch ausgelösten Sekundärelektronen.

EBISA ist ideal dazu geeignet, Streuprozesse eines fokussierten Elektronenstrahls aufgrund der Wechselwirkung mit einem (planarem) Festkörper, d.h. die Größe der Rückstreuelektronenaustrittsfläche, zu untersuchen. Bei EBISA kann eine Überlagerung von Rückstreuelektronen durch vorwärts gestreute Elektronen ausgeschlossen werden, da sich hier keine Abscheidung während der Bestrahlung mit Elektronen bildet (wie dies z.B. der Fall bei EBID ist).

Bei der Verwendung einer Membran werden Elektronenstreuprozesse reduziert, da das Elektronenwechselwirkungsvolumen „abgeschnitten“ wird. Entgegen der Erwartung konnte gezeigt werden, dass Proximity-Effekte auf einer Siliziumnitrid-Membran ausgeprägter auftreten können als auf einem dicken Substrat; dies wurde durch einen positiven Aufladungseffekt und eine dadurch ausgelöste Sauerstoff-Desorption erklärt, welche flächenmäßig die Größe der Rückstreuelektronenaustrittsfläche übersteigt. Zusätzlich wurde gezeigt, dass eine positive Aufladung des bereits abgeschiedenen Materials die EBID-Abscheiderate erhöht. Andere Erklärungsmodelle, wie z.B. Elektronenstrahl-induziertes Heizen, wurden berücksichtigt und ausgeschlossen. Diese Untersuchungen zeigen, dass bei der Verwendung von Siliziumnitrid-Membranen in Verbindung mit Elektronenstrahlen Aufladungseffekte berücksichtigt werden müssen.

Im Rahmen von Kooperationen mit der Goethe Universität Frankfurt (Prof. Dr. Michael Huth) und der Technischen Universität Wien (Prof. Dr. Alois Lugstein) wurden die Eigenschaften der Eisenabscheidungen weiter untersucht.

Leitfähigkeits- und Magnetisierungsmessungen zeigen, dass die Abscheidungen metallisch und ferromagnetisch sind. Diese Ergebnisse sind in Übereinstimmung mit der hohen Reinheit der Eisenabscheidungen, die durch die AES-Messungen bestimmt wurden. Es wurde außerdem herausgefunden, dass das autokatalytische Wachstum durch Chromoxid inhibiert werden kann. Dies ist eine weitere Möglichkeit die Morphologie der Nanostrukturen zu beeinflussen. Diese Ergebnisse zeigen deutlich, dass die Oberfläche einen signifikanten Einfluss auf den Abscheideprozess selbst haben kann, wie dies z.B. ebenfalls bei EBISA der Fall ist.

Im Rahmen der zweiten Kooperation wurde gezeigt, dass die Eisenabscheidungen als Katalysator für das Wachstum von Silizium-Nanodrähten mittels chemischer Gasphasenabscheidung (engl. high temperature chemical vapor deposition) ausgehend von dem Precursor Oktachlortrisilan,  $\text{Si}_3\text{Cl}_8$ , dienen können. Unter den verwendeten Wachstumsbedingungen wachsen die Silizium-Nanodrähte über den sogenannten „vapor-solid-solid“-Wachstumsmodus an Eisensilizid-Partikeln.

Abschließend kann bemerkt werden, dass die Ergebnisse dieser Doktorarbeit klar darauf hinweisen, dass die chemischen Eigenschaften der Oberfläche selbst eine entscheidende Rolle im Abscheideprozess spielen können, und daher im Allgemeinen berücksichtigt werden müssen.

---

---

## 7. Literature

- [1] H. Marbach, *Microscopic and Spectromicroscopic Insight and Fabrication of Nanoscaled Structures on Surfaces*, Habilitation treatise, FAU Erlangen-Nürnberg, Erlangen (2010).
- [2] M. Knoll, E. Ruska, *Z. Phys.* 78 (1932) 318.
- [3] E. Ruska E, *Bioscience rep.* 7 (1987), 607.
- [4] W. F. van Dorp, B. van Someren, C. W. Hagen, P. Kruit, *Nano Lett.* 5 (2005) 1303.
- [5] E. Platzgummer, H. Löschner, *J. Vac. Sci. Technol. B* 27 (2009) 2707.
- [6] I. Utke, P. Hoffmann, R. Berger, L. Scandella, *Appl. Phys. Lett.* 80 (2002) 4792.
- [7] A. Botman, J. J. L. Mulders, C.W. Hagen, *Nanotechnology* 20 (2009) 372001.
- [8] Y. M. Lau, P. C. Chee, J. T. L. Thong, V. Ng, *J. Vac. Sci. Technol. A* 20 (2002) 1295.
- [9] D. L. Huber, *Small* 1 (2005) 482.
- [10] K. S. Suslick, T. Hyeon, M. Fang, *Chem. Mater.* 8 (1996) 2172.
- [11] A. Moiala, A. G. Nasibulin, E. I. Kauppinen, *J. Phys.: Condens. Matter* 15 (2003) 3011.
- [12] R. L. Vander Wal, *Combust. Flame* 130 (2002) 37.
- [13] T. Lukasczyk, *Generation of pure iron nanostructures via electron-beam induced deposition in UHV*, PhD thesis, FAU Erlangen-Nürnberg, Erlangen (2010).
- [14] J. Goldstein et al., *Scanning Electron Microscopy and X-ray Microanalysis*, 3. Edition, Springer Netherlands (2002).
- [15] H. Seiler, *Z. angew. Phys.* 22 (1967) 249.
- [16] L. Reimer, *Scanning Electron Microscopy. Physics of Image Formation and Microanalysis*, Springer-Verlag Berlin Heidelberg, Berlin (1998).
- [17] L. Meitner, *Z. Phys.* 11 (1922) 35.
- [18] G. Wedler, *Lehrbuch der Physikalischen Chemie*, 5. Auflage, WILEY-VCH Verlag GmbH Co. KGaA, Weinheim (2004).
- [19] D. Briggs, M. P. Seah, *Practical Surface Analysis by Auger and X-ray Photoelectron Spectroscopy*, John Wiley & Sons, Chichester (1983).
- [20] L. C. Feldman, *Fundamentals of surface and thin film analysis*, North-Holland, New York (1986).
- [21] K. Oura, V. G. Lifshits, A. A. Saranin, A. V. Zotov, M. Katayama, *Surface Science, An Introduction*, Springer-Verlag Berlin Heidelberg New York, Heidelberg (2003).
- [22] J. F. Watts, J. Walstenholme, *An Introduction to Surface Analysis by XPS and AES*, John Wiley & Sons Ltd, Chichester (2003).

- [23] M. Schirmer, *Generation of Titanium Oxide Nanostructures via Electron Beam induced Deposition in UHV*, PhD thesis, FAU Erlangen-Nürnberg, Erlangen (2012).
- [24] M. Hesse, H. Meier, B. Zeeh, *Spektroskopische Methoden in der organischen Chemie*, 7. überarbeitete Auflage, Thieme, Wemding (2005).
- [25] S. Frabboni, G. C. Gazzadi, A. Spessot, *Physica E: Low-dimensional Systems and Nanostructures* 37 (2007) 265.
- [26] W. F. van Dorp, C. W. Hagen, *J. Appl. Phys.* 104 (2008) 081301.
- [27] I. Utke, P. Hoffmann, J. Melngailis, *J. Vac. Sci. Technol. B* 26 (2008) 1197.
- [28] S. J. Randolph, J. D. Fowlkes, P. D. Rack, *Crit. Rev. Sol. State* 31 (2006) 55.
- [29] K. Edinger, H. Becht, J. Bihr, V. Boegli, M. Budach, T. Hofmann, H.W. P. Koops, P. Kuschnerus, J. Oster, P. Spies, B. Weyrauch, *J. Vac. Sci. Technol. B* 22 (2004) 2902.
- [30] A. E. Ennos, *Brit. J. of Appl. Phys.* 4 (1953) 101.
- [31] A. N. Broers, W. W. Molzen, J. J. Cuomo, N. D. Wittels, *Appl. Phys. Lett.* 29 (1976) 596.
- [32] A. G. Baker, W. C. Morris, *Rev. Sci. Instrum.* 32 (1961) 458.
- [33] I. Utke, T. Bret, D. Laub, P. Buffat, L. Scandella, P. Hoffmann, *Microel. Eng.* 73-74 (2004) 553.
- [34] I. Utke, J. Michler, P. Gasser, C. Santschi, D. Laub, M. Cantoni, P. Th. A. Buffat, C. Jiao, P. Hoffmann, *Adv. Eng. Mater.* 7 (2005) 323.
- [35] H. W. P. Koops, C. Schössler, A. Kaya, M. Weber, *J. Vac. Sci. Technol. B* 14 (1996) 4105.
- [36] I. Utke, P. Hoffmann, B. Dwir, K. Leifer, E. Kapon, P. Doppelt, *J. Vac. Sci. Technol. B* 18 (2000) 3168.
- [37] S. Matsui, T. Ichihashi, M. Mito, *J. Vac. Sci. Technol. B* 7 (1989) 1182.
- [38] D. Drouin, A. R. Couture, D. Joly, X. Tastet, V. Aimez, R. Gauvin, *Scanning* 29 (2007) 92.
- [39] J. D. Wnuk, J. M. Gorham, S. G. Rosenberg, W. F. van Dorp, T. E. Madey, C. W. Hagen, D. H. Fairbrother, *J. Phys. Chem. C* 113 (2009) 2487.
- [40] J. D. Wnuk, J. M. Gorham, S. G. Rosenberg, W. F. van Dorp, T. E. Madey, C. W. Hagen, D. H. Fairbrother, *J. Appl. Phys.* 107 (2010) 054301.
- [41] B. C. Ibanescu, O. May, A. Monney, M. Allan, *Phys. Chem. Chem. Phys.* 9 (2007) 3163.
- [42] S. Massey, P. Cloutier, M. Bazin, L. Sanche, D. Roy, *J. Appl. Polym. Sci.* 108 (2008) 3163.
- [43] N. Silvis-Cividjian, C. W. Hagen, *Electron-beam-induced nanometer-scale deposition, Advances in Imaging and Electron Physics*, Vol. 143, Elsevier Academic Press Inc., San Diego (2006).

- 
- [44] M. L. Knotek, P. J. Feibelman, *Phys. Rev. Lett.* **40** (1978) 964.
- [45] R. R. Kunz, T. M. Mayer, *Appl. Phys. Lett.* **50** (1987) 962.
- [46] R. R. Kunz, T. E. Allen, T. M. Mayer, *J. Vac. Sci. Technol. B* **5** (1987) 1427.
- [47] R. R. Kunz, T. M. Mayer, *J. Vac. Sci. Technol. B* **6** (1988) 1557.
- [48] G. Hochleitner, H. D. Wanzenboeck, E. Bertagnolli, *J. Vac. Sci. Technol. B* **26** (2008) 939.
- [49] R. L. Kubena, F. P. Stratton, T. M. Mayer, *J. Vac. Sci. Technol. B* **6** (1988) 1865.
- [50] D. P. Adams, T. M. Mayer, B. S. Swartzentruber, *Appl. Phys. Lett.* **68** (1996) 2210.
- [51] D. P. Adams, T. M. Mayer, B. S. Swartzentruber, *J. Vac. Sci. Technol. B* **14** (1996) 1642.
- [52] F. Zaera, *Langmuir* **7** (1991) 1188.
- [53] T. N. Rhodin, C. F. Brucker, *Solid State Commun.* **23** (1977) 275.
- [54] T. N. Rhodin, C. F. Brucker, *Solid State Commun.* **17** (1975) 391.
- [55] L. J. E. Hofer, E. Sterling, J. T. McCartney, *J. Phys. Chem.* **59** (1955) 1153.
- [56] D. W. Moon, D. J. Dwyer, S. L. Bernasek, *Surf. Sci.* **163** (1985) 215.
- [57] M.-M. Walz, M. Schirmer, F. Vollnhals, T. Lukasczyk, H.-P. Steinrück, H. Marbach, *Angew. Chem. Int. Ed.* **49** (2010) 4669.
- [58] D. P. Adams, L. L. Tedder, T. M. Mayer, B. S. Swartzentruber, E. Chason, *Phys. Rev. Lett.* **74** (1995) 5088.
- [59] D. P. Adams, T. M. Mayer, E. Chason, B. K. Kellerman, B. S. Swartzentruber, *Surf. Sci.* **371** (1997) 445.
- [60] H. D. Hagstrum, *J. Chem. Phys.* **23** (1955) 1178.
- [61] M. A. Fineman, A. W. Petrocelli, *J. Chem. Phys.* **36** (1962) 25.
- [62] P. C. Engelking, W. C. Lineberger, *J. Am. Chem. Soc.* **101** (1979) 5569.
- [63] R. H. Schultz, K. C. Crellin, P. B. Armentrout, *J. Am. Chem. Soc.* **113** (1991) 8590.
- [64] H. H. Madden, *J. Vac. Sci. Technol.* **13** (1976) 228.
- [65] M.-L. Shek, S. P. Withrow, W. H. Weinberg, *Surf. Sci.* **72** (1978) 678.
- [66] Sigma Aldrich, *safety data sheet iron pentacarbonyl*, Steinheim (2011).
- [67] Omicron NanoTechnology, *Multiscan STM VT User's Guide*, Vol. 1, Taunusstein (2005) 12.
- [68] M. Schirmer, *Lithographic Fabrication of Nanostructures by Means of Electron-Beam Induced Deposition (EBID)*, Master thesis, FAU Erlangen-Nürnberg, Erlangen (2006).
- [69] M. L. Knotek, J. E. Houston, *J. Vac. Sci. Technol. B* **1** (1983) 899.
- [70] H. Niehus, W. Losch, *Surf. Sci.* **111** (1981) 344.

## 7. Literature

---

- [71] T. Lukasczyk, M. Schirmer, H.-P. Steinrück, H. Marbach, *Langmuir* 25 (2009) 11930.
- [72] C. N. R. Rao, G. U. Kulkarni, P. J. Thomas, P. P. Edwards, *Chem. Eur. J.* 8 (2002) 28.
- [73] A. F. Holleman, E. Wiberg, N. Wiberg, Holleman-Wiberg, *Lehrbuch der Anorganischen Chemie*, vol. 101, Walter de Gruyter & Co., Berlin (1995).
- [74] W. Zhang, M. Shimojo, M. Takeguchi, K. Furuya, *J. Mater. Sci.* 41 (2006) 2577.
- [75] G. Hollinger, F. J. Himpsel, *Appl. Phys. Lett.* 44 (1984) 93.
- [76] M. Morita, T. Ohmi, E. Hasegawa, M. Kawakami, M. Ohwada, *J. Appl. Phys.* 68 (1990) 1272.
- [77] R. M. Glaeser, K. H. Downing, *Microsc. Microanal.* 10 (2004) 790.
- [78] K. H. Downing, M. R. McCartney, R. M. Glaeser, *Microsc. Microanal.* 10 (2004) 783.
- [79] V. A. Gritsenko, I. P. Petrenko, S. N. Svitashva, H. Wong, *Appl. Phys. Lett.* 72 (1998) 462.
- [80] V. A. Gritsenko, H. Wong, J. B. Xu, R. M. Kwok, I. P. Petrenko, B. A. Zaitsev, Yu. N. Morokov, Yu. N. Novikov, *J. Appl. Phys.* 86 (1999) 3234.
- [81] K. A. Nasyrov, S. S. Shaimeev, V. A. Gritsenko, J. H. Han, C. W. Kim, J.-W. Lee, *J. Exp. Theor. Phys.* 102 (2006) 810.
- [82] V. A. Gritsenko, *Phys. Uspekhi* 52 (2009) 869.
- [83] I. A. Chaiyasena, P. M. Lenahan, G. J. Dunn, *J. Appl. Phys.* 72 (1992) 820.
- [84] E. Suzuki, Y. Hayashi, K. Ishi, T. Tsuchiya, *Appl. Phys. Lett.* 42 (1983) 608.
- [85] A. P. Aganin, V. M. Maslovskii, A. P. Nagin, *Microelectronics* 17 (1988) 348.
- [86] Z. A. Weinberg, K. J. Stein, T. N. Nguen, J. Y. Sun, *Appl. Phys. Lett.* 57 (1990) 1248.
- [87] M.-M. Walz, F. Vollnhals, M. Schirmer, H.-P. Steinrück, H. Marbach, *Phys. Chem. Chem. Phys.* 13 (2011) 17333.
- [88] V. Gopal, E. A. Stach, V. R. Radmilovic, *Appl. Phys. Lett.* 85 (2004) 49.
- [89] Y. R. Choi, P. D. Rack, S. J. Randolph, D. A. Smith, D. C. Joy, *Scanning* 28 (2006) 311.
- [90] T. Bret, I. Utke, P. Hoffmann, M. Aboudira, P. Doppelt, *Microelectron. Eng.* 83 (2006) 1482
- [91] J. V. B. Oriedo, D. H. Russell, *J. Phys. Chem.* 96 (1992) 5314.
- [92] C. W. Hagen, W. F. Van Dorp, P. A. Crozier, *J. Phys.: Conf. Ser.* 126 (2008) 012025.
- [93] M. Song, K. Mitsuishi, M. Tanaka, M. Takeguchi, M. Shimojo, K. Furuya, *Appl. Phys. A* 80 (2005) 1431.
- [94] S. K. de Boer, W. F. van Dorp, J. Th. M. de Hosson, *J. Vac. Sci. Technol. B* 29 (2011) 06FD01.

- 
- [95] M. Shimojo, M. Takeguchi, M. Tanaka, K. Mitsuishi, K. Furuya, *Appl. Phys. A* 79 (2004) 1869.
- [96] M. Shimojo, M. Takeguchi, R. Che, W. Zhang, M. Tanaka, K. Mitsuishi, K. Furuya, *Japan. J. Appl. Phys.* 45 (2006) 5509.
- [97] A. Fernandez-Pacheco, J. M. De Teresa, R. Cordoba, M. R. Ibarra, *J. Appl. Phys. D* 42 (2009) 055005.
- [98] M. Rubinstein F. J. Rachford, W. W. Fuller, G. A. Prinz, *Phys. Rev. B* 37 (1988) 8689.
- [99] S. J. Raeburn, R. V. Aldridge, *J. Phys. F: Met. Phys.* 8 (1978) 1917.
- [100] Y. K. Kim, M. Oliveria, *J. Appl. Phys.* 74 (1993) 1233.
- [101] P. J. Cumpson, M. P. Seah, *Surf. Interface Anal.* 25 (1997) 430.
- [102] G. Ertl, *Angew. Chem.* 120 (2008) 3578.
- [103] M. G. Jenke, D. Lerose, C. Niederberger, J. Michler, S. Christiansen, I. Utke, *Nano Lett.* 11 (2011) 4213.
- [104] V. Schmidt, J. V. Wittemann, U. Gösele, *Chem. Rev.* 110 (2010) 361.
- [105] I. Ahmad, M. Fay, Y. Xia, X. Hou, A. Kennedy, Y. Zhu, *J. Phys. Chem. C* 113 (2009) 1286.
- [106] V. Schmidt, S. Senz, U. Gösele, *Z. Metallkund.* 96 (2005) 427.
- [107] N. Fukata, T. Oshima, T. Tsurui, S. Ito, K. Murakami, *Sci. Technol. Adv. Mater.* 6 (2005) 628.
- [108] R. J. Barsotti, Jr., J. E. Fischer, C. H. Lee, J. Mahmood, C. K. W. Adu, P. C. Eklund, *Appl. Phys. Lett.* 81 (2002) 2866.
- [109] Z. Q. Liu, S. S. Xie, W. Y. Zhou, L. F. Sun, Y. B. Li, D. S. Tang, X. P. Zou, C. Y. Wang, G. Wang, *J. Cryst. Growth* 224 (2001) 230.
- [110] A. M. Morales, C. M. Lieber, *Science* 279 (1998) 208.
- [111] A. Enders, R. Skomski, J. Honolka, *J. Phys.: Condens. Matter* 22 (2010) 433001.

---

## 8. Abbreviations

AGDT	<b>A</b> dditional <b>G</b> as <b>D</b> osage <b>T</b> ime	ms	<b>m</b> ultiple <b>s</b> weep
AES	<b>A</b> uger <b>E</b> lectron <b>S</b> pectroscopy	n	<b>n</b> umber of sweeps
AE	<b>A</b> uger <b>E</b> lectron	N	<b>N</b> itrogen
AFM	<b>A</b> tomical <b>F</b> orce <b>M</b> icroscope/y	O	<b>O</b> xygen
AG	<b>A</b> utocatalytic <b>G</b> rowth	os	<b>o</b> ne <b>s</b> weep
ARB	<b>A</b> R <b>B</b> itrary waveform generator	PE	<b>P</b> rimary <b>E</b> lectron
Au	gold (lat. <b>A</b> urum)	RT	<b>R</b> oom <b>T</b> emperature
BSE	<b>B</b> ack <b>S</b> cattered <b>E</b> lectron	SAM	<b>S</b> canning <b>A</b> uger electron <b>M</b> icroscopy
C	<b>C</b> arbon	sccm	<b>s</b> tandard <b>c</b> ubic <b>c</b> entimeters per <b>m</b> inute
CEM	<b>C</b> hannel <b>E</b> lectron <b>M</b> ultiplier	SE	<b>S</b> econdary <b>E</b> lectron
Cr	<b>C</b> hromium	SEM	<b>S</b> canning <b>E</b> lectron <b>M</b> icroscope/y
CVD	<b>C</b> hemical <b>V</b> apor <b>D</b> eposition	Si	<b>S</b> ilicon
d	electron <b>d</b> ose	ss	<b>s</b> tep <b>s</b> ize
DAC	<b>D</b> igital-to- <b>A</b> nalog <b>C</b> onverter	STM	<b>S</b> canning <b>T</b> unneling <b>M</b> icroscope/y
DC	<b>D</b> irect <b>C</b> urrent	$t_{dw}$	<b>d</b> well <b>t</b> ime
DD	<b>D</b> ipolar <b>D</b> issociation	TEM	<b>T</b> ransmission <b>E</b> lectron <b>M</b> icroscope/y
DEA	<b>D</b> issociative <b>E</b> lectron <b>A</b> ttachment	UHV	<b>U</b> ltra- <b>H</b> igh <b>V</b> acuum
DI	<b>D</b> issociative <b>I</b> onization	$U_{PE}$	<b>P</b> E beam acceleration voltage
EBID	<b>E</b> lectron <b>B</b> eam <b>I</b> nduced <b>D</b> eposition	QMS	<b>Q</b> uadrupole <b>M</b> ass <b>S</b> pectrometer/ <b>m</b> etry
EBIE	<b>E</b> lectron <b>B</b> eam <b>I</b> nduced <b>E</b> tching	Z	atomic number
EBISA	<b>E</b> lectron <b>B</b> eam <b>I</b> nduced <b>S</b> urface <b>A</b> ctivation	$\rho$	density
EDX	<b>E</b> nergy <b>D</b> ispersive <b>X</b> -ray		
EI	<b>E</b> lectron <b>I</b> mpact		
ESD	<b>E</b> lectron <b>S</b> timulated <b>D</b> esorption		
EUV	<b>E</b> xtrême <b>U</b> ltra <b>V</b> iolet		
Fe	Iron (lat. <b>F</b> errum)		
FEBIP	<b>F</b> ocused <b>E</b> lectron <b>B</b> eam <b>I</b> nduced <b>P</b> rocessing		
FEL	<b>F</b> ast <b>E</b> ntry <b>L</b> ock		
FSE	<b>F</b> orward <b>S</b> cattered <b>E</b> lectron		
HV	<b>H</b> igh <b>V</b> acuum		
$I_{PE}$	<b>P</b> E beam current		
K	<b>K</b> elvin		
LEED	<b>L</b> ow <b>E</b> nergy <b>E</b> lectron <b>D</b> iffraction		
$E_{PE}$	<b>P</b> E beam <b>E</b> nergy		

---

## 9. Acknowledgment

Hereby, I would like to thank and acknowledge the following persons for supporting me throughout my thesis and for contributing to the results of this work.

In particular, I am grateful to my supervisors **Prof. Dr. Hans-Peter Steinrück**, for giving me the opportunity to work at his chair, for the numerous fruitful discussions and the great support, and **PD Dr. Hubertus Marbach**, for interesting, valuable discussions and for always taking the time to support me with helpful ideas and input.

For second assessment I thank **PD Dr. Norbert Jux**.

Thanks to **the EBID Team, Dr. Thomas Lukasczyk, Michael Schirmer, Florian Vollnhals and Florian Rietzler**, for creating such a creative working atmosphere. I really enjoyed working with you!

For good and fruitful collaborations, I would like to thank our **cooperation partners Prof. Dr. Michael Huth, Dr. Fabrizio Poratti, Roland Sachser** (Institute for Physics, Goethe-University Frankfurt, Germany).

**Prof. Dr. Emmerich Bertagnolli, Ass.-Prof. Dr. Alois Lugstein & co-workers** (Institute for Solid State Electronics, Technical University Vienna, Austria).

**Prof. Dr. Paul Müller, Dr. Yuri Koval, Klaus Gieb, Wolfgang Kröner** (Department of Physics, University Erlangen-Nürnberg, Germany).

For **technical support**, which is one of the most important things when working with such a multitude of equipment, I gratefully acknowledge **Hans-Peter Bäumlner, Bernd Kreß** and **Friedhold Wölfel and all the members of the mechanical workshop**.

For **financial support** I acknowledge the **Graduate School Molecular Science**.

**All the members of the Chair of Physical Chemistry II** I thank for the great working atmosphere.

Finally, I would like to thank especially **my family, Evelyn Walz, Dr. Walter Kotrba, Dr. Marion Kotrba, Samuel Walz, Leopold Walz and Dr. Alexander Haueis**, who supported me not only throughout my thesis in manifold ways, but also throughout my studies.

---

## 10. Curriculum Vitae

Marie-Madeleine Walz (M.Sc.)

Born August 10<sup>th</sup> 1983 in Erlangen, Germany

### University

- from 2008/06     **Dissertation**  
at the Chair of Physical Chemistry II (Prof. Dr. Hans-Peter Steinrück)  
in the “Microscopy and Nanolithography” group (Dr. Hubertus Marbach)  
at the Friedrich-Alexander-University (FAU) Erlangen-Nürnberg.
- 2008/05     **Master of Science**  
*Thesis:* “Fabrication of Titanium Oxide Nanostructures on Au(111) via  
Electron-Beam Induced Deposition (EBID)”
- 2006/08     **Bachelor of Science**  
*Thesis:* “Direkte Synthese von Zn-Tetraphenylporphyrin auf einem  
Ag(111)-Einkristall”
- 2003/10     **Molecular Science / Molecular Nano Science (BSc / MSc) Studies**  
- 2008/05     at the FAU Erlangen-Nürnberg

### School

- 2000-2003     Gymnasium Steigerwald Landschulheim in Wiesentheid  
“Abitur und Erwerb der allgemeinen Hochschulreife” (2003)
- 1999-2000     Städt. Johannes – Scharrer Gymnasium in Nürnberg
- 1995-1999     Realschule der Englischen Fräulein in Bamberg  
“Mittlere Reife“ (1999)
- 1993-1995     Zentral – Volksschule in Forchheim
- 1989-1993     Martin - Volksschule in Forchheim

---

## 11. Peer-reviewed publications

- (9) ***Investigation of Proximity Effects in Focused Electron Beam Induced Processing***  
**M.-M. Walz**, F. Vollnhals, F. Rietzler, M. Schirmer, A. Kunzmann, H.-P. Steinrück, H. Marbach  
*Journal of Physics D: Applied Physics*, in press.
- (8) ***Investigation of Proximity Effects in Electron Microscopy and Lithography***  
**M.-M. Walz**, F. Vollnhals, F. Rietzler, M. Schirmer, H.-P. Steinrück, H. Marbach  
*Applied Physics Letters* 100 (2012) 053118.
- (7) ***Fabrication of Layered Nanostructures by Successive Electron Beam Induced Deposition with Two Precursors: Protective Capping of Metallic Iron Structures***  
M. Schirmer, **M.-M. Walz**, C. Papp, F. Kronast, A. X. Gray, B. Balke, S. Cramm, C. S. Fadley, H.-P. Steinrück, H. Marbach  
*Nanotechnology* 22 (2011) 475304.
- (6) ***Magnetotransport Properties of Iron Microwires Fabricated by Focused Electron Beam Induced Autocatalytic Growth***  
F. Porrati, R. Sachser, **M.-M. Walz**, F. Vollnhals, H.-P. Steinrück, H. Marbach, M. Huth  
*Journal of Physics D: Applied Physics* 44 (2011) 425001.
- (5) ***Generation of Clean Iron Nanocrystals on an Ultra-Thin SiO<sub>x</sub> Film on Si(001)***  
**M.-M. Walz**, F. Vollnhals, M. Schirmer, H.-P. Steinrück, H. Marbach  
*Physical Chemistry Chemical Physics* 13 (2011) 17333.
- (4) ***Electron Beam Induced Deposition and Post Treatment Processes to Locally Generate Clean Titanium Oxide Nanostructures on Si(100)***  
M. Schirmer, **M.-M. Walz**, F. Vollnhals, Th. Lukasczyk, A. Sandmann, Ch. Chen, H.-P. Steinrück, H. Marbach  
*Nanotechnology* 22 (2011) 085301.
- (3) a ***Electrons as “Invisible Ink”: Fabrication of Nanostructures by Local Electron Beam Induced Activation of SiO<sub>x</sub>***  
**M.-M. Walz**, M. Schirmer, F. Vollnhals, Th. Lukasczyk, H.-P. Steinrück, H. Marbach  
*Angewandte Chemie International Edition* 49 (2010) 4669.  
(Very Important Paper (VIP), cover page, featured e.g. in *Nature Materials* 5 (2010) 476 and *New Scientist* issue 2765)

## 11. Peer-reviewed publications

---

- b ***Elektronen als “Unsichtbare Tinte”:* Herstellung von Nanostrukturen durch Lokale Elektronenstrahlinduzierte Aktivierung von SiO<sub>x</sub>**  
**M.-M. Walz**, M. Schirmer, F. Vollnhals, Th. Lukasczyk, H.-P. Steinrück, H. Marbach  
*Angewandte Chemie* 122 (2010) 4774.
- (2) ***Tetraphenylporphyrin Picks up Zinc Atoms from a Silver Surface***  
A. Kretschmann, **M.-M. Walz**, K. Flechtner, H.-P. Steinrück, J. M. Gottfried  
*Chemical Communications* 6 (2007) 568.
- (1) ***Surface-Confined Two-Step Synthesis of the Complex (Ammine)(meso-tetraphenylporphyrinato)-zinc(II) on Ag(111)***  
K. Flechtner, A. Kretschmann, L. R. Bradshaw, **M.-M. Walz**, H.-P. Steinrück, J. M. Gottfried  
*Journal of Physical Chemistry C* 111 (2007) 5821.

### ***Additional Publications***

- (1) ***An Alternative to FIB - Direct Writing with an Electron-Beam in UHV: Lithographic Fabrication of Clean Iron Nanostructures***  
Th. Lukasczyk, M. Schirmer, **M.-M. Walz**, F. Vollnhals, H.-P. Steinrück, H. Marbach  
*Omicron Pico* 12 (2008) 6.

## 12. Appendix

- P1** [\*\*Electrons as “Invisible Ink”: Fabrication of Nanostructures by Local Electron Beam Induced Activation of SiO<sub>x</sub>\*\*](#)  
**Marie-Madeleine Walz**, Michael Schirmer, Florian Vollnhals, Thomas Lukasczyk, Hans-Peter Steinrück, Hubertus Marbach  
*Angewandte Chemie International Edition* 49 (2010) 4669 (VIP).
- P2** [\*\*Generation of Clean Iron Nanocrystals on an Ultra-Thin SiO<sub>x</sub> Film on Si\(001\)\*\*](#)  
**Marie-Madeleine Walz**, Florian Vollnhals, Michael Schirmer, Hans-Peter Steinrück, Hubertus Marbach  
*Physical Chemistry Chemical Physics* 13 (2011) 17333.
- P3** [\*\*Investigation of Proximity Effects in Electron Microscopy and Lithography\*\*](#)  
**Marie-Madeleine Walz**, Florian Vollnhals, Florian Rietzler, Michael Schirmer, Hans-Peter Steinrück, Hubertus Marbach  
*Applied Physics Letters* 100 (2012) 053118.
- P4** [\*\*Investigation of Proximity Effects in Focused Electron Beam Induced Processing\*\*](#)  
**Marie-Madeleine Walz**, Florian Vollnhals, Florian Rietzler, Michael Schirmer, Andreas Kunzmann, Hans-Peter Steinrück, Hubertus Marbach  
*Journal of Physics D: Applied Physics*, in press.
- P5** [\*\*Magnetotransport Properties of Iron Microwires Fabricated by Focused Electron Beam Induced Autocatalytic Growth\*\*](#)  
Fabrizio Porrati, Roland Sachser, **Marie-Madeleine Walz**, Florian Vollnhals, Hans-Peter Steinrück, Hubertus Marbach, Michael Huth  
*Journal of Physics D: Applied Physics* 44 (2011) 425001.

This is a cumulative dissertation with the full text of the scientific publications in the *Appendix*. Due to copyright protection, the dissertation pdf file in the internet must not contain the full text but the citations of the publications.